




OATAO is an open access repository that collects the work of Toulouse researchers and makes it freely available over the web where possible

This is an author's version published in: <http://oatao.univ-toulouse.fr/27004>

Official URL:

<https://doi.org/10.1016/j.ymsp.2020.106880>

To cite this version:

Al Janaideh, Mohammad and Al Saaideh, Mohammad and Rakotondrabe, Micky  *On hysteresis modeling of a piezoelectric precise positioning system under variable temperature.* (2020) *Mechanical Systems and Signal Processing*, 145. 1-27. ISSN 0888-3270

Any correspondence concerning this service should be sent to the repository administrator: tech-oatao@listes-diff.inp-toulouse.fr

On Hysteresis Modeling of a Piezoelectric Precise Positioning System Under Variable Temperature

Mohammad Al Janaideh, Mohammad Al Saaideh, and Micky Rakotondrabe

M. AL JANAIDEH is with the Department of Mechanical Engineering, Memorial University, St. John's,

Newfoundland A1B 3X5, Canada, maljanaideh@mun.ca

M. AL SAAIDEH is with the Department of Electrical Engineering, The University of Jordan, Amman, Jordan, moh990saaideh@gmail.com

M. RAKOTONDRABE is with Laboratoire Génie de Production, National School of Engineering in Tarbes (ENIT) / Toulouse INP, University of Toulouse, Tarbes France, mrakoton@enit.fr.

Abstract

We propose the modeling of hysteresis nonlinearities in a piezoelectric material-based tube actuator classically employed in precise positioning applications under different surrounding temperatures. Beyond the voltage-to-displacement hysteresis nonlinearities they exhibit, these actuators are sensitive to the surrounding temperature. Therefore, contrary to the existing works in the literature where the two phenomena were treated individually, this paper suggests to model the hysteresis nonlinearities and the temperature effects simultaneously. First an experimental study was performed to investigate the effects of the surrounding temperature on the voltage-to-displacement hysteresis loops of the piezoelectric tube actuators. The experimental results show that increasing the input surrounding temperature contributes an increase in the voltage-to-displacement sensitivity of the piezoelectric tube actuator under the input voltage range considered in the experimental tests. Then, two different nonlinear temperature-dependent hysteresis models a temperature-dependent (TD) electromechanical model and a temperature-dependent Prandtl-Ishlinskii model (TD-PI) were proposed to account the temperature effects on the hysteresis nonlinearity. In First, the mathematical formulation of TD-electromechanical model was presented to describe the electrical and mechanical properties of piezoelectric tube actuator. This model integrates the temperature dependent electromechanical coupling factor to model the temperature effects, the Simscape library in MATLAB-Simulink software was used to develop a physical simulation for the TD-electromechanical model. In a second time, a TD-PI model was proposed

to describe the voltage-to-displacement characteristic of piezoelectric tube actuator using a proposed temperature shape function. The parameters of the two proposed models were estimated using proposed optimization algorithms based on Grey Wolf Optimizer (GWO). The modeling results demonstrate that the two proposed models can account for the hysteresis nonlinearities of the piezoelectric tube actuators under different levels of the surrounding temperatures. Finally, the analytical inverse of TD-PI model was derived and applied in feed forward manner to compensate the hysteresis nonlinearities under different levels of the surrounding temperatures.

keyword: Piezoelectric, Temperature dependent, Positioning, Hysteresis, Prandtl-Ishlinskii, Electromechanical Model.

1 Introduction

Piezoelectric material-based actuators have been recently used in different precise positioning systems since they can perform high resolution of movement at high excitation frequencies. Precise positioning driven by piezoelectric materials are found in various applications and some of them are now commercially available [1]. For example, these applications include the Atomic Force Microscopy (AFM) [2, 3], manipulator applications [4, 5, 6], piezoelectrically actuated hydraulic valves [7], diesel injectors [8], medical microrobots [9]. Different hysteresis models have been used to characterize the voltage-to-displacement hysteresis nonlinearities in piezoelectric material-based actuators over different operating conditions have been presented in a number of recent studies, see for example [10, 11, 12, 13, 14]. In [10], the both rate-independent and rate-dependent hysteresis in piezoelectric actuators were modeled using a Takagi–Sugeno fuzzy system. As compared to another fuzzy-based modeling methods, their method can be used for online modeling and the inverse can be obtained analytically. In [11], the non-saturation hysteresis model for piezo-bender actuator was presented. The hysteresis model was obtained based on geometrical deformation of main hysteresis loop for online modeling. In [12], a dynamic hysteresis model which describes the hysteresis effect, creep effect, electrical and mechanical vibration dynamics was proposed for flexure-guided piezo platform. In [13], a novel method based on the combination of particle swarm optimization algorithm with discrete Presiach model was proposed to represent a simplified procedure for hysteresis modeling of a piezoelectric actuator. In [14], the hysteresis nonlinearities were modeled using a fractional order differential model where the input of the model was modified voltage with extraction of a linear time-delayed component.

Whilst the high attention in hysteresis modeling and control of piezoelectric actuators, most

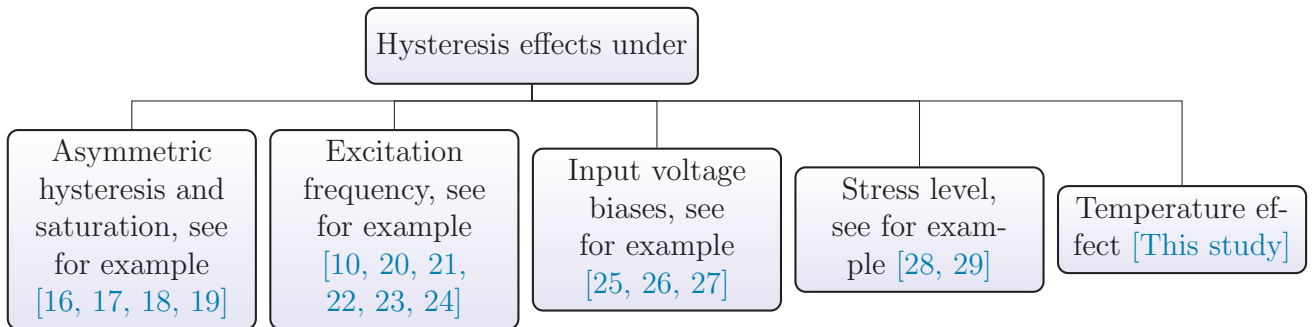


Figure 1: Hysteresis nonlinearities under different conditions.

of the available studies present the hysteresis nonlinearities modeling under different conditions as represented in Figure 1. However, beyond their strong hysteresis nonlinearities, these actuators also exhibit high sensitivity to the variation of the surrounding temperature [15] and very few works were devoted to them.

The main objective of different hysteresis models is to propose control techniques that can reduce the inaccuracies in the output displacement due to these nonlinearities. These models include lumped parameter electromechanical models and operator-based hysteresis models. The lumped parameter electromechanical models use a physical electromechanical representation to characterize electromechanical properties and hysteresis of piezoelectric material-based actuators, while the operator-based hysteresis models use phenomenological nonlinear operators with memory effects to characterize Input-output hysteresis loops of piezoelectric material-based actuators [30, 31].

Goldfarb and Celanovic proposed the first lumped parameter electromechanical model that describes the dynamics and the voltage-to-displacement hysteresis of piezoelectric material-based actuators for control applications [32]. Their model is implemented with a Maxwell-slip model and a physical model of two ports of interactions: a voltage-current port in the electrical part that represented by the equivalent capacitance of piezoelectric material, and a force-velocity port in the mechanical part that represented by single mass-spring-damper system. In [33], the electromechanical model was developed with Duhem model to describe the hysteresis nonlinearities and a partial differential equation in the mechanical part of the model to characterize the dynamic behavior of piezoelectric actuator. The piezoelectric effect of the two models in [32] and [33] was formulated using an electromechanical coupling factor between electrical side and mechanical side.

In [34], a resistance element has been added to the electrical part of the electromechanical model to consider the dynamics of a piezoelectric actuator system under the effects of load, peak voltage, and frequency of the input voltage. The model in [34] has been developed in [35] using

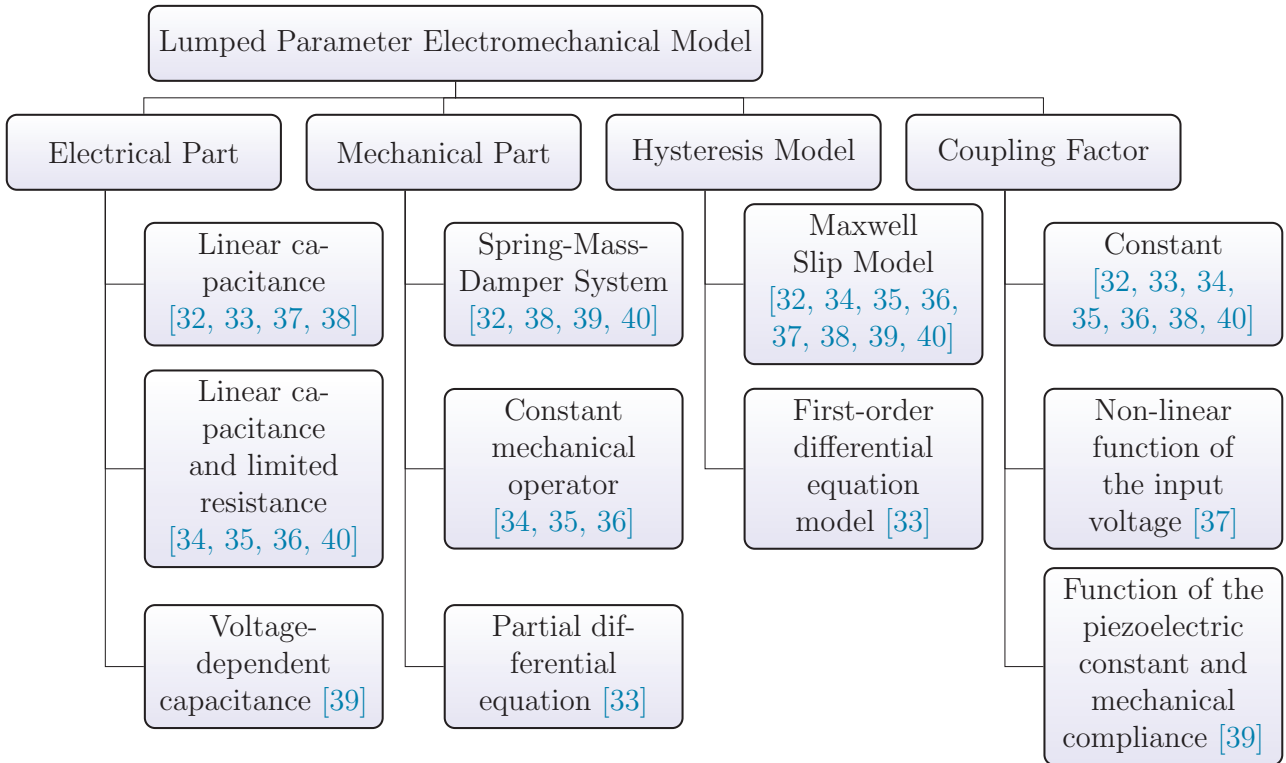


Figure 2: The proposed Electromechanical Model in the literature review.

the Maxwell-slip model which relates the charge to the applied voltage across the piezoelectric actuator. In [35], the compliance of the piezoelectric material (of the actuator) is used to consider a mechanical operator that represents the effects of the external load on the actuator system. In later work, the model in [35] was extended to describe the drift behavior of piezoelectric actuator by integrating a series of resistance-capacitor circuits in the electrical part of model [36]. Later on, the electromechanical model in [32] has been developed in a number of studies, see for example [37, 38, 39, 40]. In [37], the electromechanical model was developed with a generalized Maxwell-slip model and a non-linear coupling factor between electrical part and mechanical part. In [38], an identification technique was proposed to identify the parameters of the electromechanical model. In [39] a voltage-dependent capacitance equivalent was proposed to enhance a performance of the electromechanical model. In [40], the electromechanical model was proposed for a micro-positioning system that consists of a piezoelectric actuator and a flexure mechanism. The summary of the electromechanical model is presented in Figure 2.

The Prandtl-Ishlinskii model has been proposed to describe the hysteresis nonlinearities in elasto-plastic materials [41]. The Prandtl-Ishlinskii is nonlinear model that uses the play hysteresis

operator to model hysteresis nonlinearities in smart material-based actuators which include piezoelectric material-based actuators and magnetostrictive material-based actuators [42]. Piezoelectric material-based actuators exhibit creep, asymmetric voltage-to-displacement hysteresis loops, and rate-dependent hysteresis loop [1]. To characterize hysteresis nonlinearities of piezoelectric material-based actuators under different conditions, the Prandtl-Ishlinskii model with several modifications has been proposed in different studies, see for example [43, 44, 45, 46]. In [43], an explicit integral formula was added to the model to propose a creep operator that characterizes the hysteresis and creep nonlinearities and compensates the hysteresis nonlinearities in different micro-positioning applications, see for example [47]. In [44], the Generalized Prandtl-Ishlinskii was proposed to model asymmetric hysteresis loops of piezoelectric material-based actuators with saturation nonlinearity when the amplitude of the input exceeds a certain limit. In [45], a dynamic threshold function is used in the play hysteresis operator to model the rate-dependent hysteresis nonlinearities of a piezoelectric material-based actuator over different excitation frequencies. A Hammerstein system consists the Prandtl-Ishlinskii model with a linear dynamical systems was used to model the dynamics of piezoelectric actuator [46, 48].

The effect of the temperature on piezoelectric actuators behavior could be drastically in the final tasks if not properly accounted. For instance, piezoelectric tube actuators, called piezotube scanners, are the main actuator used for scanning probe microscopy for images scanning [49], and are also used in precise positioning for nano-indentation [50], nano-manipulation or nano-assembly [51, 52]. In these applications, the tasks are generally under lights allowing the cameras that track them to record efficiently. Due to the small sizes of the environment, the lights greatly modifies the surrounding temperature and can increase it up to $10^{\circ}C$ relative in one hour [53]. Understanding the effect of the temperature on the behavior of piezoelectric actuators is therefore essential as it allows to further model and lessen this effect.

The temperature effects on piezoelectric materials were investigated experimentally in a number of studies [54, 55, 56, 57]. The experimental results for these studies show that the dielectric and piezoelectric constants of the piezoelectric materials increase as the temperature increases within a certain range. In [54], the intrinsic and domain-wall contributions properties of two ceramic materials were determined directly and quantitatively using experimental methodology under temperature dependence. The experimental results of [54] show massive change in the dielectric and piezoelectric constants when temperature increases temperature. In [55], the temperature dependence of dielectric and piezoelectric constants such as (d_{33}, d_{31}, k_{31}) for Perovskite materials, Polycrystalline ceramics, and single crystals is obtained under two different temperatures. The experimental results show increasing in dielectric constants as temperature increases.

In [56], the temperature dependence of the dielectric constant, electromechanical coupling coefficient, and frequency constant for two single crystals materials under two temperature cycles were proposed. The experimental results show increasing in these constants with the temperatures below the transition temperature, then the unstable behavior was observed for high temperatures. In [57], the temperature dependence of the dielectric permittivity constant, the piezoelectric constant, the elastic rigidity constant, and the elastic compliance constant were assumed to have a parabolic function of temperature based on the experimental results investigated in [56].

The effects of the surrounding temperature, however, on the hysteresis properties of piezoelectric material-based actuators are generally ignored because the experimental measurement are usually conducted in the laboratories where the temperature level is controlled [58], or where a feedback control of the actuator is designed to reject minor effects of the temperature disturbance [59]. In a recent study [60], the temperature variation was potentially exploited to also excite the piezoelectric actuator, then a hybrid thermo-piezo based actuator was proposed.

The main contributions of this work are as follows:

- Study the temperature effects on the hysteresis loops of a piezoelectric tube actuator. This is essential to evaluate and understand the uncertainties caused by the temperature effects on the piezoelectric tube actuator model and consequently the effect on precise positioning tasks.
- Develop a lumped parameter electromechanical model that characterizes the voltage-to-displacement hysteresis under different surrounding temperatures. This model proposed a temperature-dependent coupling factor to present the interactions between the temperature effects and the elements (mechanical and electrical elements) of the electromechanical model.
- Propose a Temperature-Dependent Prandtl-Ishlinskii model that considers the temperature effects on the voltage-to-displacement hysteresis loops. This model is essential for model-based control system that could use the inverse model as a feedforward compensator to reduce the effects of the hysteresis nonlinearities with the uncertainties due to the temperature effects.

The proposed study supports recent studies in the area of high-precision systems that use piezoceramic actuators for motion control and micro-positioning applications. These include Atomic Force Microscope, design of micro-positioning manipulator-based piezoceramic actuators, flow control with piezoceramic actuators, and fuzzy-modeling of piezoceramic actuators. For Atomic Force Microscope, see for example [3], the proposed models can enhance that nanoscale measurement and manipulation of the piezoceramic actuators when these actuators are operated in the Atomic

Force Microscope under different environmental temperatures. Specifically, the proposed nonlinear models can be implemented with the motion control systems of the piezoceramic actuators of the Atomic Force Microscope to enhance the accuracy of the piezoceramic actuators. For the design of positioning manipulator-based piezoceramic actuators, the proposed nonlinear models can enhance the precision tracking control of these manipulators [4, 5, 6, 11, 12, 13, 14, 16, 19, 24]. For example, the positioning accuracy of the ultramicroscopic imaging can be enhanced by considering the uncertainties due to the temperature effects in piezoceramic actuators [6]. This could minimize the overall positioning errors of the ultramicroscopic imaging. The proposed models can develop the applications of the piezoceramic actuator in hydraulic- and pneumatic-piezoceramic valves. Specifically, the proposed models can provide uncertainties of fluid flow in hydraulic- and pneumatic-piezoceramic valves due to the temperature effects [7, 8]. For fuzzy-based hysteresis models that consider the frequency of the input voltage as a factor in hysteresis modeling [5, 10], the effect of environmental temperatures can be considered as a new factor to enhance the application of these hysteresis models in modeling the nonlinear dynamics of the piezoceramic actuators.

The remaining parts of this paper are formulated as follows: Section 2 presents an experimental study to study the hysteresis nonlinearities of a piezoelectric tube actuator under different surrounding temperatures. The proposed Temperature-dependent Electromechanical model is formulated in Section 3. Section 4 presents the proposed Temperature-dependent Prandtl-Ishlinskii (TD-PI) model. The optimization algorithm and parameters identification procedures of the proposed models with simulation results are introduced in Section 5. In Section 6, the analytical inverse of temperature-Dependent Prandtl-Ishlinskii (TD-PI) is derived. The conclusion and future work are summarized in Section 7.

2 Experimental Study

This section presents a description of the experimental platform that was used to explore the effects of surrounding temperature on the voltage-to-displacement hysteresis nonlinearities of a piezoelectric tube actuator. The main objective is to investigate the effects of the surrounding temperature on the magnitude and the sensitivity (mean slope) of the voltage-to-displacement hysteresis loop of the piezoelectric tube actuator.

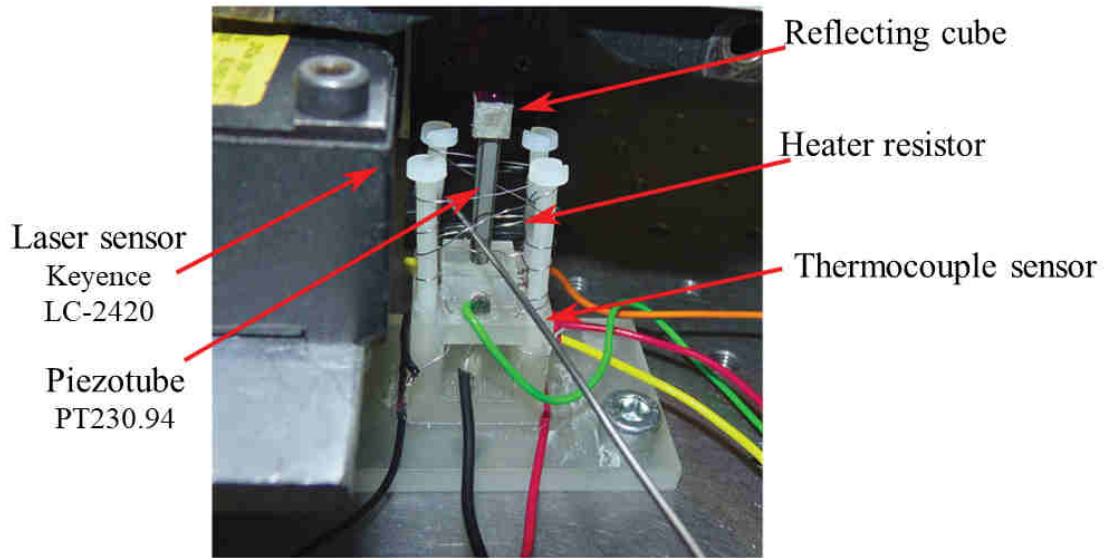
2.1 The experimental setup of the piezoelectric tube actuator

The proposed smart actuator is a piezoelectric actuator with tubular structure and can be called as piezoelectric tube (or piezotube) actuator, it is classically employed in Atomic Force Microscopy (AFM) and Nano-indentation. The Piezotube actuator is a PT230.94 from Physik Instrumente of 27 mm active length, 5 mm diameter and 3 mm inner diameter. A heater resistor controlled by an electrical current i_T is used to control the temperature T in the vicinity of the actuator while a laser sensor is placed in the front of the extremity of the actuator to measure the displacement y . The used laser sensor is a LC-2420 from Keyence company with a precision of a hundred nanometers and 10 kHz bandwidth. The probe of a thermocouple sensor is integrated inside the heater resistor in order to measure the temperature T in the vicinity of the actuator. Finally, a computer with the MATLAB-Simulink software is used to generate all the input signals (v_s and i_T) and to acquire the output measurements (T and y). The computer includes an acquisition board dS1103 (from dSPACE) with digital to analog converters (ADC and DAC).

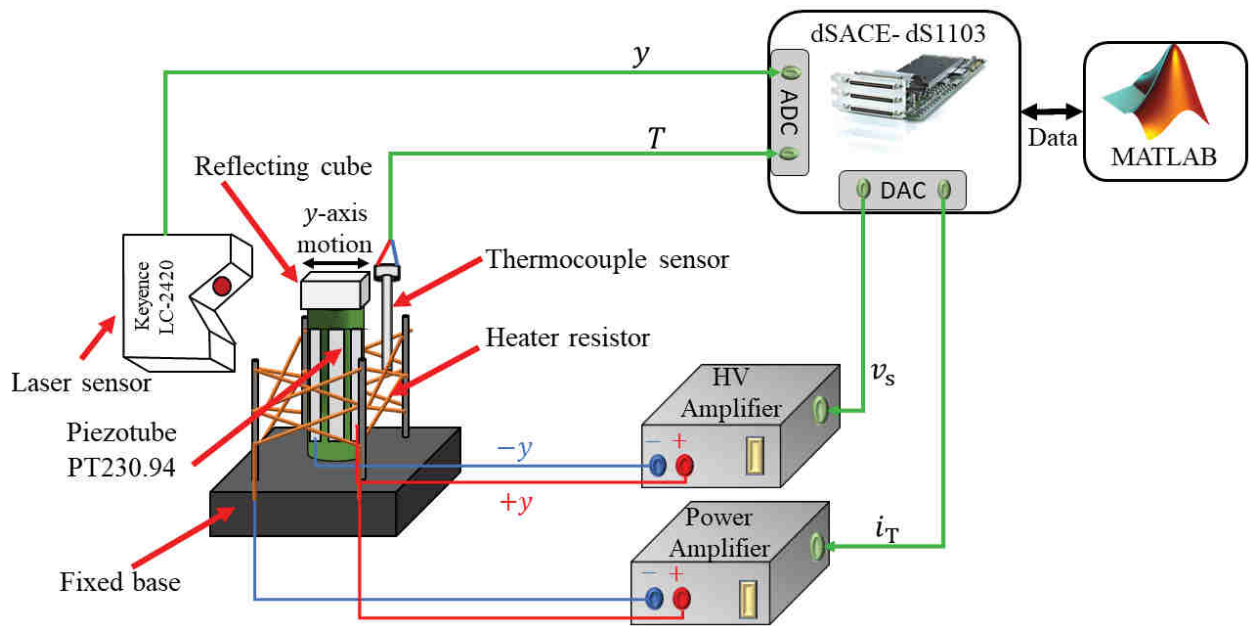
Since the generated excitation input signals (voltage and current) from the computer are limited to ± 10 V and to ± 20 mA due to dSPACE requirement, a High-voltage (HV) amplifier of (up to ± 200 V) and a Power Amplifier of (up to 4 A) are placed between the DAC of dSPACE and both the piezoelectric tube actuator and the heater resistor, respectively. The data acquisition system sampling time is set to $t_s = 0.2$ ms. [Figure 3 \(a\)](#) displaces piezotube actuator with its surrounding components and [Figure 3 \(b\)](#) displays a schematic diagram with the main components of the experimental platform.

2.2 Characterization of hysteresis nonlinearities under different surrounding temperatures

The hysteresis nonlinearities of the piezoelectric tube actuator are characterized by applying a harmonic input voltage $v_s(t) = 200 \sin(2\pi ft)$ V of frequency $f = 0.1$ Hz at different input surrounding temperatures of $T = 23^\circ\text{C}$, 29°C , 33°C , 35°C , and 39°C . The range of temperature is chosen approximately of 10°C relative from the ambient temperature of 20°C to 39°C . This corresponds to the classical case when a piezoelectric tube actuator is used for micro/nano-positioning task that requires the use of light to assist the camera for recording. In these tasks, the temperature raises from ambient to 10°C more in one hour due to the light [\[53\]](#). Therefore we used the heater to impose the selected temperatures of $T = 23^\circ\text{C}$, 29°C , 33°C , 35°C , and 39°C . The voltage-to-displacement hysteresis loops of the piezoelectric tube actuator under these temperatures are illustrated in [Figure 4](#). The figure shows that increasing the surrounding temperature yields an



(a)



(b)

Figure 3: The experimental platform: (a) The piezotube actuator with its surrounding components (laser displacement sensor, thermocouple sensor, heater), and (b) Schematic diagram of the entire experimental setup.

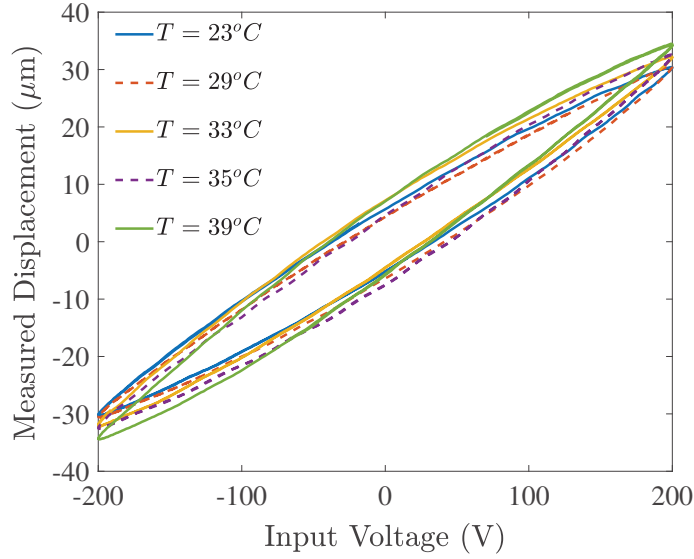


Figure 4: The measured voltage-to-displacement hysteresis loops due to a harmonic input voltage $v_s(t) = 200 \sin(2\pi ft)$ V of frequency $f = 0.1$ Hz at different input surrounding temperatures of $T = 23^\circ C$, $29^\circ C$, $33^\circ C$, $35^\circ C$, and $39^\circ C$

increase in the sensitivity (mean slope) of the actuator within the temperature levels considered during the experimental tests. This sensitivity can be evaluated using the mean slope of the best linear-line model of the hysteresis loop as represented by the red-line in Figure 5 (a). The sensitivities of all hysteresis loops are calculated as $0.1509 \mu m/V$, $0.1523 \mu m/V$, $0.1606 \mu m/V$, $0.1627 \mu m/V$, and $0.1735 \mu m/V$ for the surrounding temperatures $T = 23^\circ C$, $29^\circ C$, $33^\circ C$, $35^\circ C$, and $39^\circ C$, respectively. The sensitivity (mean slope) of the voltage-to-displacement is presented in Figure 5 (b) as a function of the surrounding temperature T that is applied to the piezoelectric tube actuator. The figure illustrates that increasing the surrounding temperature T contributes an increase in the sensitivity (mean slope) of the piezoelectric tube actuator within the selected input surrounding temperatures.

3 Temperature-Dependent (TD) Electromechanical Model

Different lumped parameter electromechanical models with number of improvements and modifications have been proposed to describe the electrical and mechanical behavior of piezoelectric actuator [34, 36, 37, 40]. This section develops an electromechanical model with temperature-dependent effect. In order to present the electrical properties of the piezoelectric tube actuator,

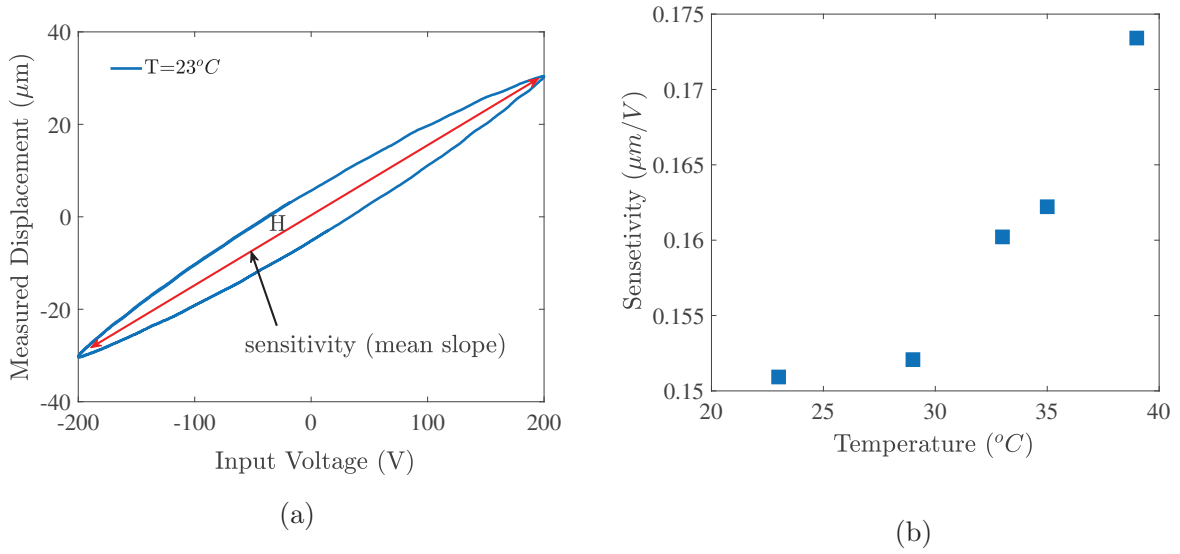


Figure 5: (a) Representation of the best linear-line model (H) for hysteresis loop which was used to calculate the sensitivity (mean slope), and (b) The sensitivity (mean slope) of the piezoelectric tube actuator under different levels of surrounding temperature: $T = 23^\circ\text{C}$, 29°C , 33°C , 35°C , and 39°C .

an equivalent capacitance C in parallel with limited resistance R are used. These values of these elements vary with the applied voltage, external load, and excitation frequency of the applied input voltage [34]. The mechanical properties of piezoelectric tube actuator are presented using the equivalent mass-spring-damper system. The values of these elements depend on the types and the dimensions of the used piezoelectric materials. These elements are connected as the schematic representation in Figure 6 to form the proposed TD-electromechanical model of piezoelectric tube actuator.

In this model, the hysteresis model $H(v_s)$ is proposed to characterize the relationship between the current \dot{q} feeds in the piezoelectric tube actuator and the applied voltage v_s . The current \dot{q}_p produced from the estimated velocity \dot{y} of the mechanical part is subtracted from the source current \dot{q} and the remaining current flows in the electrical part that is represented by the equivalent capacitance C parallel to the limited Resistance R . The mechanical part of the proposed model is presented by mass-spring-damper elements where the input force F is produced from the linear voltage v_p across the equivalent capacitance in electrical part. The piezoelectric effect between the electrical part and mechanical part is represented by electromechanical coupling factor $\psi(T)$ which is proposed to has function of surrounding temperature T .

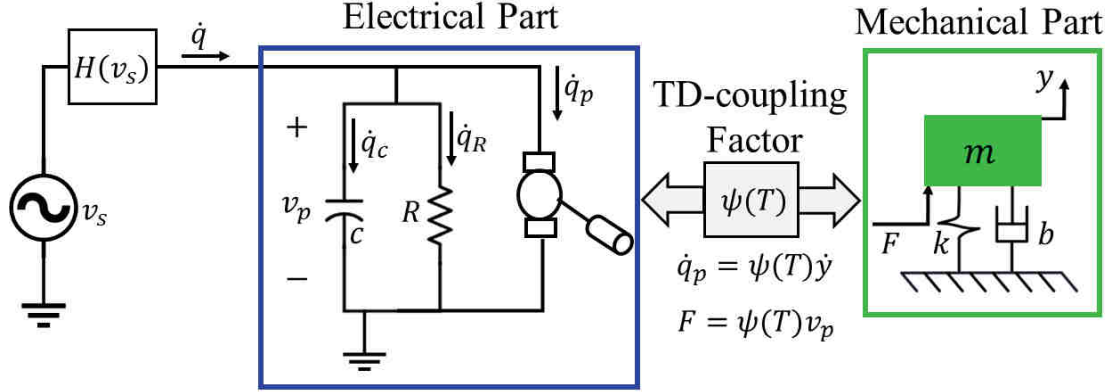


Figure 6: Schematic representation of the proposed TD electro-mechanical model for the piezoelectric tube actuator, where v_s is the input applied voltage, $H(v_s)$ is Maxwell-slip hysteresis model, \dot{q} is the total current in the actuator, \dot{q}_c is the current in the equivalent capacitance C , \dot{q}_R is the current in the limited resistor R , \dot{q}_p is the produced current from the mechanical part, m is the mass, b is the damping factor, k is the stiffness, F is the produced force from the electrical part, and $\psi(T)$ is the proposed temperature-dependant coupling factor.

3.1 Temperature-dependent coupling factor

The electromechanical models of piezoelectric actuator in the literature used a constant coupling factor, see for example [32, 35]. This factor depends on the piezoelectric constant and mechanical compliance as $\psi = \frac{d_{33}A}{s_{33}t_p}$ [39], where d_{33} is the piezoelectric constant, s_{33} is the mechanical compliance, A actuator cross sectional area, and t_p is the layer thickness. However, different studies from physical perspectives proposed that the piezoelectric constant d_{33} increases as the temperature increases [54, 55, 56]. In [57], this constant is assumed to has a parabolic function of temperature. Considering these results, the coupling factor ψ can be expressed to consider the temperature effects as

$$\psi(T) = \frac{d_{33}(T)A}{s_{33}(T)t_p}, \quad (1)$$

where $d_{33}(T)$ and $s_{33}(T)$ are function of temperature T . This factor represents the key of the proposed TD-electromechanical model in this study.

3.2 Formulation of the TD-electromechanical model

This section develops the mathematical formulation of TD-electromechanical model considering the temperature-dependent coupling factor. The electrical part of model is formulated as follows

$$\dot{q}(t) = H(v_s(t)), \quad (2)$$

where $\dot{q}(t)$ is the total current feeds in the piezoelectric tube actuator and $v_s(t)$ is the voltage applied to the piezoelectric tube actuator, and H is Maxwell-slip hysteresis nonlinearites model. Then, the nodal current equation is written as

$$\dot{q}(t) = \dot{q}_c(t) + \dot{q}_R(t) + \dot{q}_p(t), \quad (3)$$

where $\dot{q}_c(t)$ is the current of equivalent capacitance C , $\dot{q}_R(t)$ is the current of limited resistor R , and $\dot{q}_p(t)$ is the produced current from the mechanical part. These currents are expressed as

$$\begin{aligned} \dot{q}_c(t) &= c\dot{v}_p(t), \\ \dot{q}_R(t) &= \frac{v_p(t)}{R}, \\ \dot{q}_p(t) &= \psi(T)\dot{y}_E(t), \end{aligned} \quad (4)$$

where $\psi(T)$ is the proposed temperature-dependant coupling factor, $v_p(t)$ is the linear voltage across the equivalent capacitance, and $y_E(t)$ is the output displacement of the TD-electromechanical model. By substituting Equation (4) into Equation (3), we obtain

$$\dot{q}(t) = c\dot{v}_p(t) + \frac{v_p(t)}{R} + \psi(T)\dot{y}_E(t). \quad (5)$$

The mechanical part of the model TD-electromechanical is formulated as:

$$m\ddot{y}_E(t) + b\dot{y}_E(t) + ky_E(t) = F(t), \quad (6)$$

where m is the mass, b is the damping coefficient, k is the stiffness coefficient of the piezoelectric tube actuator, $y_E(t)$ is the output displacement of the TD-electromechanical model, and F is the produced force from the electrical part and can be expressed as

$$F(t) = \psi(T)v_p(t), \quad (7)$$

where $\psi(T)$ is the coupling factor function of temperature T and v_p is the linear voltage across the equivalent capacitance. Then we can obtain the transfer function $G(s)$ between the actuator current $\dot{q}(t)$ and the output displacement $y_E(t)$ as

$$G(s) = \frac{Y_E(s)}{\dot{Q}(s)} = \frac{\psi(T)}{mcs^3 + (bc + \frac{m}{R})s^2 + (kc + \frac{b}{R} + \psi^2(T))s + \frac{k}{R}}. \quad (8)$$

The TD-electromechanical model is represented by hysteresis model and linear transfer function as illustrated using block diagram representation in Figure 7. The hysteresis behavior between the input voltage $v_s(t)$ and the current $\dot{q}(t)$ is represented using Maxwell-slip hysteresis model as used in the different electromechanical models for the piezoelectric actuators.

3.3 Simulation of TD-electromechanical model

The TD-electromechanical model shown in Figure 6 is implemented using Physical modeling library (Simscape) in MATLAB-Simulink software. The model is represented using three sub-models: the Maxwell slip hysteresis model, electrical model, and mechanical model as shown in Figure 8. In this model, the coupling factor $\psi(T)$ between the electrical and mechanical models is considered as function of surrounding temperature.

As shown in Figure 8, the electrical model is represented by two elements: capacitor C and resistor R connected to two current sources. The two current source blocks are used to model the current $\dot{q}(t)$ from the Maxwell-slip hysteresis block and the current $\dot{q}_p(t)$ produced from the mechanical model. The voltage $v_p(t)$ across the capacitance C is obtained using the voltage sensor block.

The mechanical model shown in Figure 8 is represented by three elements: mass m , damper b , and spring k . The input force block is used to model the force $F(t)$ produced from the electrical model and the output displacement $y_E(t)$ is obtained using the position sensor block. The interaction between the electrical and mechanical models is formulated using the electromechanical coupling factor which is a function of surrounding temperature. Finally, the hysteresis nonlinearities in the TD-electromechanical model is implemented using the Maxwell-slip model [32].

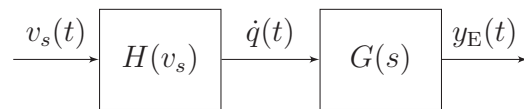


Figure 7: Block diagram representation of TD-electro-mehcanical model, where $v_s(t)$ is the input voltage, $H(v_s)$ is the Maxwell-slip hysteresis model, $\dot{q}(t)$ is the current, $G(s)$ is a transfer function that represents the relationship between the input current $\dot{q}(t)$ and the output displacement $y_E(t)$ as Equation (8).

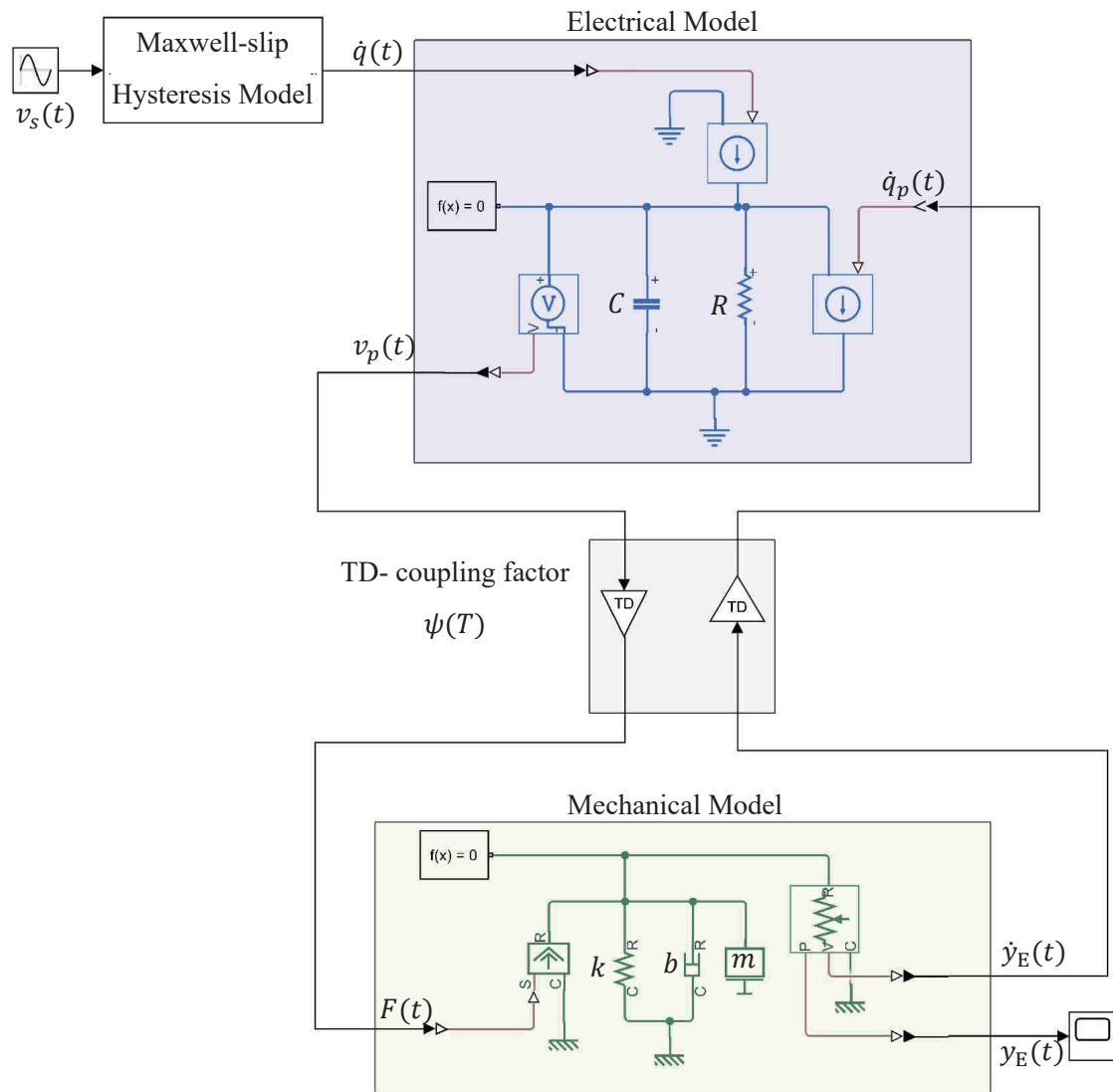


Figure 8: Simulink with Simscape elements representation of the TD-electromechanical model.

4 Temperature-Dependent Prandtl-Ishlinskii Model

Describing the hysteresis behavior of the above piezoelectric tube actuator under surrounding temperature variation necessitates the development of a hysteresis model which is parameterized by the temperature effect. Compared to other hysteresis models, the Prandtl-Ishlinskii one offers flexible mathematical formulation which allows defining the model parameters (threshold and weighting functions in this case) on the basis of the experimental factors such as input rate, bias or stress levels. This section presents a description of the mathematical formulation of the

Prandtl-Ishlinskii model with a temperature-dependent feature.

4.1 Formulation of the TD-PI hysteresis model

The Temperature-Dependent Prandtl-Ishlinskii (TD-PI) model is constructed with the play operator of a threshold r and input $v_s(t)$. For an input $v_s(t) \in C_m[0, T]$ that is monotone in subinterval $[t_{k-1}, t_k]$ where C_m is the space of the piecewise monotone continuous function and $0 = t_0 < t_1 < \dots < t_N = T$ are intervals in $[0, T]$, the output of the play operator $\mathcal{F}_r[v_s](t)$ in subinterval $[t_{k-1}, t_k]$ where $0 \leq k \leq (N - 1)$ and for a given threshold $r > 0$, is defined by the formula:

$$\mathcal{F}_r[v_s](t_k) = \max(v_s(t_k) - r, \min(v_s(t_k) + r, \mathcal{F}_r[v_s](t_{k-1}))) \quad (9)$$

with initial condition

$$\mathcal{F}_r[v_s](0) = \max(v_s(0) - r, \min(v_s(0) + r, 0)).$$

The output of the TD-PI model can be expressed as

$$\mathcal{P}[v_s, \bar{T}](t) = \int_0^R p(r, \bar{T}) \mathcal{F}_r[v_s](t) dr, \quad (10)$$

where $\bar{T} = T - T_o$ is the variation in the temperature and $p(r, \bar{T})$ is a weight function of threshold r such that $p(r, \bar{T}) = 0$ for $r > R$, where R is a positive constant.

It is essential to obtain the shape function of the TD-PI model. This function determines the shape of the hysteresis loop and it is used to derive the inverse model. The temperature-shape function can be defined as

$$\phi(r, \bar{T}) = p_0 r + \int_0^r p(\tau_r, \bar{T})(\tau_r - r) d\tau_r. \quad (11)$$

where $p_0 = p(0, \bar{T})$ is a positive constant that depends on the variation of the temperature. Then, we derive the density function:

$$\frac{\partial^2 \phi(r, \bar{T})}{\partial r^2} = \phi''(r, \bar{T}) = p(r, \bar{T}). \quad (12)$$

The weights of the density function can be identified using the experimental results and an optimization algorithm. The optimization algorithm and parameters identification procedures are

explained in details in Section 5. Let

$$p(r, \bar{T}) = p_T(\bar{T})p_r(r), \quad (13)$$

where $p_T(\bar{T})$ and $p_r(r)$ are positive integrable weighting functions that can be identified based on the experimental results. Then

$$\phi(r, \bar{T}) = p_0 r + p_T(\bar{T}) \int_0^r p_r(\tau_r)(\tau_r - r) d\tau_r. \quad (14)$$

We use another presentation for the model in Equation (10) to identify the parameters of the TD-PI model

$$\mathcal{P}_T[v_s](t) = \phi'_r(0)p_{0T}u(t) + \int_0^R \phi''_r(r)\mathcal{F}_r[v_s](t)dr, \quad (15)$$

where $\phi'(0) = p_{0r}$. Consequently, the temperature-shape function can be expressed as

$$\mathcal{P}_T[v_s](t) = p_T(\bar{T}) \int_0^R p_r(r)\mathcal{F}_r[v_s](t)dr. \quad (16)$$

Finally, the continuous form of the TD-PI model can be re-expressed as

$$\mathcal{P}_T[v_s](t) = \phi'(0)p_{0T}v_s(t) + p_T(\bar{T}) \int_0^R \phi''_r(r)\mathcal{F}_r[v_s](t)dr. \quad (17)$$

Since $\phi''(r, \bar{T}) = p(r, \bar{T})$, we consider

$$\phi''_r(r) = p_r(r)$$

and

$$\phi''(r, \bar{T}) = p_T(\bar{T})p_r(r).$$

4.2 The discrete TD-PI hysteresis model

This section presents the proposed TD-PI model in the discrete form, which is primary for parameters identification and inverse model formulation. The output of the discrete TD-PI model that integrates a shape-temperature function can be expressed as

$$\mathcal{P}_T[v_s](t) = \phi'_r(0)p_{0T}v_s(t) + p_T(\bar{T}) \sum_{i=1}^n \phi''_r(r_i)\mathcal{F}_r[v_s](t), \quad (18)$$

$$\phi'_T(r_i) = p_0 + p_T(\bar{T}) \sum_{i=1}^n p(r_i), \quad (19)$$

and

$$\phi''_{T_j}(r_i) = p(r_i, \bar{T}_j). \quad (20)$$

Then, the output of the discrete TD-PI model can be also expressed as

$$\mathcal{P}_T[v_s](t) = p_0 v_s(t) + p_T(\bar{T}) \sum_{i=1}^n p_r(r_i) \mathcal{F}_{r_i}[v_s](t), \quad (21)$$

where $p_0 = p_{0r} p_{0T}$ is a positive constant.

The experimental results show that the hysteresis magnitudes are relatively identical in the range of the temperature was considered in the experimental study. This implies that the threshold function of the model is independent from the temperature. Unlike the hysteresis magnitude, the actuator's sensitivity (mean slope) showed a strong dependence on the input temperature level. Thus, increasing the temperature in the vicinity of the actuator contributes to an increase in the sensitivity (mean slope) of the actuator. Furthermore, the results reveal that the pattern of increase is exponential as shown [Figure 5 \(b\)](#) depicts. Since the weighting function governs the sensitivity (mean slope) of the TD-PI model, the proposed weighting function can be formulated as

$$p(r_i, \bar{T}_j) = p_T(\bar{T}_j) p_r(r_i) = \epsilon e^{\eta(T_j - T_o)} p_r(r_i). \quad (22)$$

Let $p_T(\bar{T}_j) = \epsilon e^{\eta(T_j - T_o)}$, where ϵ and η are positive constants to be identified through the measured data, T_o is the ambient temperature and T_j is the tested input temperature. The suggested weighting function guarantees the increase in the sensitivity (mean slope) when the surrounding temperature increases. Then, at T_j , the output of TD-PI model is given by

$$\mathcal{P}_{T_j}[v_s](t) = p_0 v_s(t) + \epsilon e^{\eta(T_j - T_o)} \sum_{i=1}^n p_r(r_i) \mathcal{F}_{r_i}[v_s](t). \quad (23)$$

This model is proposed in the next section to describe the temperature-dependent hysteresis nonlinearities of piezoelectric tube actuator.

The TD-PI hysteresis model shows similar increasing and decreasing curves because of the input-output properties of the play operator [\[44\]](#). Similar to [\[44\]](#), we add envelope functions in order to develop the model for hysteresis nonlinearities modeling. Then, the output of the play

operator with the envelope function $\mathcal{F}_{\gamma_r}[v_s](t)$ in subinterval $[t_{k-1}, t_k]$ is

$$\mathcal{F}_{\gamma_r}[v_s](t_k) = \max\left(\gamma_l(v_s(t_k)) - r, \min\left(\gamma_r(v_s(t_k)) + r, \mathcal{F}_{\gamma_r}[v_s](t_{k-1})\right)\right), \quad (24)$$

where $\gamma_l(v_s(t_k)) = a_0 v_s(t_k) + a_1$ and $\gamma_r(v_s(t_k)) = b_0 v_s(t_k) + b_1$ are the linear envelope functions, where a_0 , a_1 , b_0 , and b_1 are coefficients to be identified through the experimental data and the optimization algorithm with $a_0 > 0$ and $b_0 > 0$. Then, the output of the discrete the proposed TD-PI hysteresis model at T_j can be expressed as

$$y_{\text{PI}}(t) = \mathcal{P}_{T_j}[v_s](t) = p_0 v_s(t) + \epsilon e^{\eta(T_j - T_o)} \sum_{i=1}^n p_r(r_i) \mathcal{F}_{\gamma_{r_i}}[v_s](t). \quad (25)$$

The parameters identification of the two proposed models is presented in the following section.

5 Parameters Identification for Proposed Models

The measured measured voltage-to-displacement hysteresis loops illustrated in [Figure 4](#) are used to identify the parameters of the proposed TD-electromechanical model and TD-PI hysteresis model. We consider the hysteresis loops at temperatures $T_j = [23, 33, 39]^{\circ}\text{C}$ are used for identification of the proposed models where $T_o = 23^{\circ}\text{C}$, while the hysteresis loops at temperatures $T_j = [29, 35]^{\circ}\text{C}$ are used for testing and validation of the proposed models.

5.1 Parameters identification of TD-electromechanical model

The proposed algorithm for parameters identification of the proposed TD-electromechanical model is represented by the flowchart in [Figure 9](#) and described by the following steps:

- **Step 1:**

Using the physical properties of the piezoelectric tube actuator (PT230.94) the mass is calculated as $m = 0.0026442 \text{ kg}$. The experimental tests show that the dynamic behavior of piezoelectric tube actuator can be represented by the natural frequency $w_n = 5004 \text{ rad/sec}$ and damping ratio $\zeta = 0.0357$ these two values are used to calculate the stiffness and damping coefficients of actuator as $k = 6.62107 \times 10^4 \text{ N/m}$ and $b = 0.9453015 \text{ N.s/m}$.

- **Step 2:**

The parameters of the proposed TD-electromechanical model are C , R , and $\psi(T_0)$, in addition to the parameters of the Maxwell-slip hysteresis model that is represented by the

deadband width $d = \{d_1, d_2, \dots, d_{10}\}$ and the segment slope values $g = \{g_1, g_2, \dots, g_{10}\}$. These parameters represented by the vector $X = \{C, R, \psi(T_o), d_1, d_2, \dots, d_{10}, g_1, g_2, \dots, g_{10}\}$ are selected to minimize the error the is given by Mean Square Error (MSE) as

$$\theta(T_o) = \frac{1}{N} \sum_{k=1}^N (y(t_k) - y_E(t_k))^2, \quad (26)$$

where $y(t_k)$ is the measured output displacement and $y_E(t_k)$ is the TD-electromechanical model output obtained by the Simscape model.

• **Step 3:**

After determine the best parameters of the TD-electromechanical model at the ambient temperature $T_0 = 23^\circ C$, the values of TD-coupling factor $\psi(T_j)$ are estimated at each surrounding temperature $T_j = [33, 39]^\circ C$ to minimize the error $\theta(T_j)$.

In this work, Grey Wolf Optimizer (GWO) is used for parameters identifications of TD-electromechanical model. GWO is a new metaheuristic algorithm with advantages such as: few parameters, simplicity of implementation, no derivation information is required in the initial search, and strike the right balance between the exploration and exploitation during the search [61]. GWO has been proposed in different engineering and science fields for example: global optimization, power engineering, bioinformatics, environmental applications, machine learning, networking and image processing [62]. In general, GWO simulates the two main behaviors of the grey wolves society: the leadership hierarchy behavior and the hunting behaviors. The position of grey wolf in search space represents a candidate solution X for the optimization problem. In the parameters identifications of TD-electromechanical model problem, the candidate represents the identified parameters as $X = \{C, R, \psi(T_o), d_1, d_2, \dots, d_{10}, g_1, g_2, \dots, g_{10}\}$.

The schematic representation of GWO behaviors is illustrated in Figure 10 . In the leadership hierarchy behavior, the error θ in Equation (26) is calculated for all grey wolves (candidate solutions), then the grey wolves are sorted according to the calculated error from minimum to maximum. The grey wolf with minimum error is X_a and the grey wolves with next minimum error are X_b and X_c . The rest of grey wolves are X_w . In the hunting behavior, the optimal solution of the problem is indicated according to the positions of best solutions X_a , X_b and X_c . Then, GWO updates the current solution based on the best solutions using the following two steps:

1. Calculate the distances D between each solution X_w and the best solutions in the search

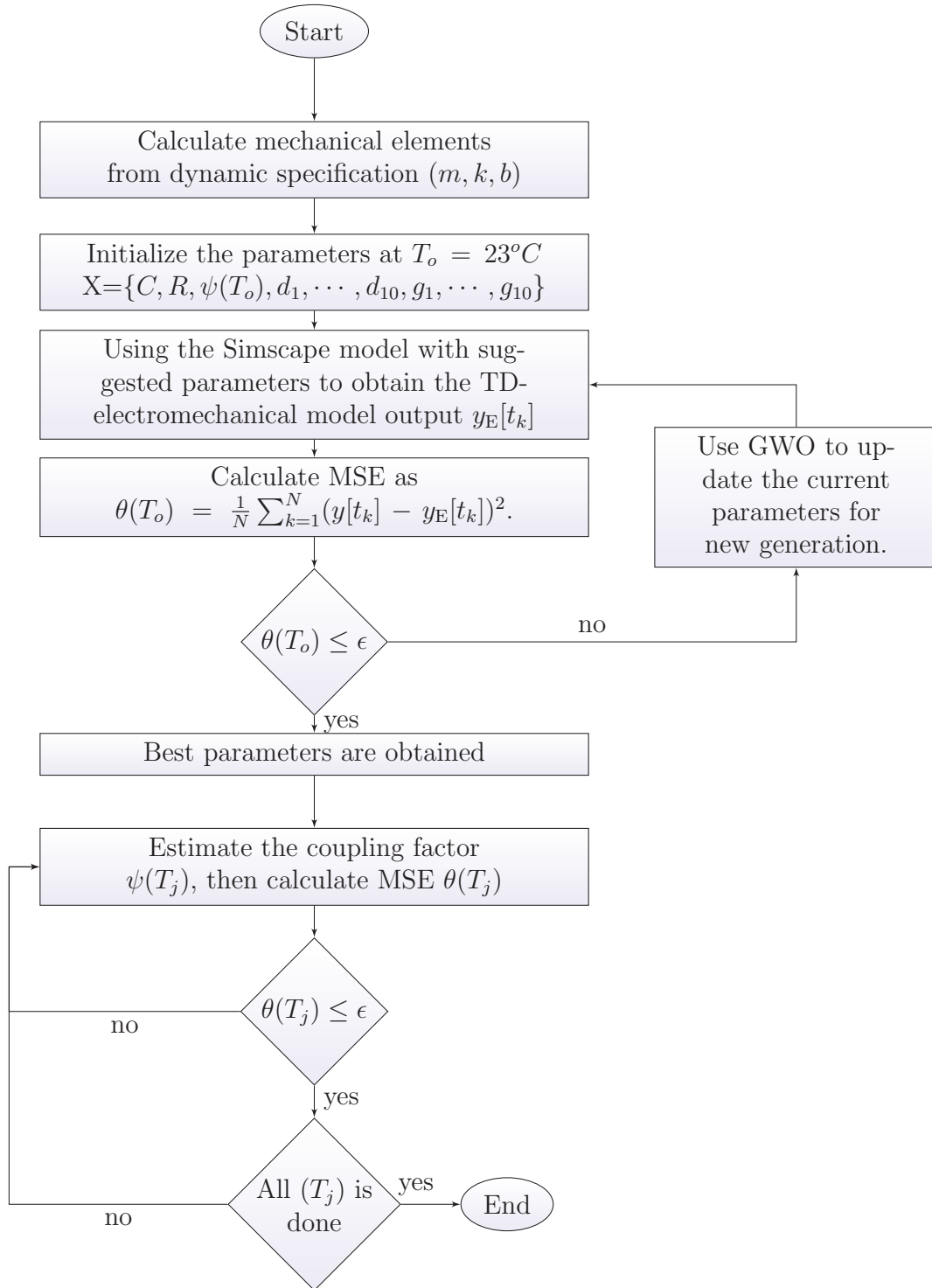


Figure 9: Flow chart of the proposed algorithm for parameters identification of the TD-electromechanical model.

space as:

$$D_a = |(2.r_1).X_a - X^g|, \quad (27a)$$

$$D_b = |(2.r_2).X_b - X^g|, \quad (27b)$$

$$D_c = |(2.r_3).X_c - X_\omega^g|, \quad (27c)$$

where X_a, X_b, X_c are the best obtained solutions, g is the index of generation, r_1, r_2 and r_3 are random numbers within $[0, 1]$.

2. Update the current position of each grey wolf X_ω as:

$$X_1 = X_a - A_1.D_a, \quad (28a)$$

$$X_2 = X_b - A_2.D_b, \quad (28b)$$

$$X_3 = X_c - A_3.D_c, \quad (28c)$$

and

$$X_\omega^{g+1} = \frac{X_1 + X_2 + X_3}{3}, \quad (29)$$

where A_1, A_2 and A_3 are the constant coefficient are calculated as $A = 2.a.r - a$ with a being linearly decreased from 2 to 0 over the generation and r is random number within $[0,1]$.

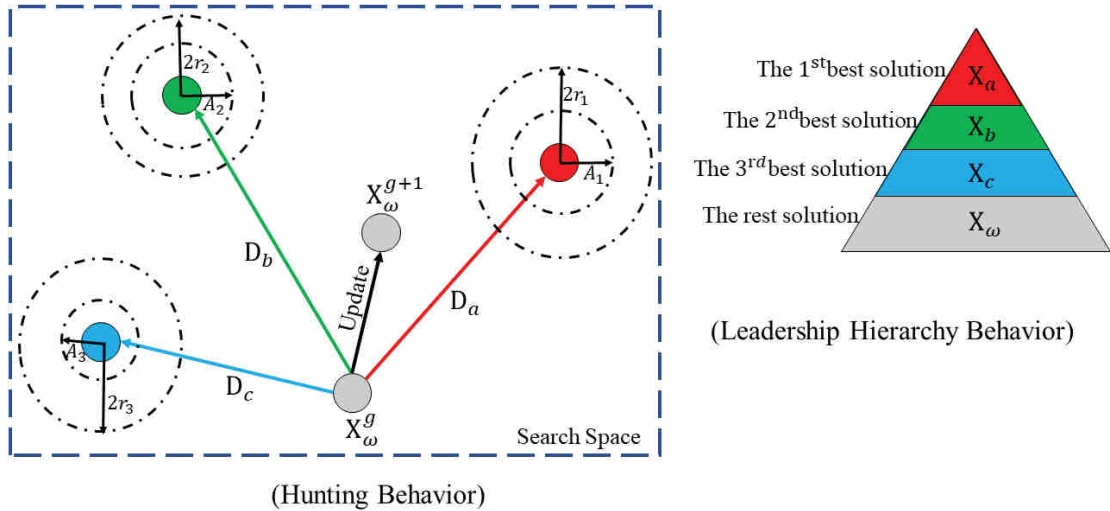


Figure 10: Schematic representation of Grey Wolf Optimizer behaviors and solution updating.

The GWO algorithm is implemented in MATLAB software and the output of TD-electromechanical model is obtained using the Simscape model. The estimated parameters of TD-electromechanical

model are obtained as follows: the equivalent capacitance $C = 48.65 \mu F$, the limited resistance $R = 21.6879 \Omega$, and the coupling factor values for surrounding temperatures $T = 23, 33,$ and $39 \text{ }^\circ\text{C}$ are estimated as $\psi = 7.2971 \times 10^{-4}, 7.7782 \times 10^{-4},$ and 8.4007×10^{-4} , respectively. Figure 11 shows that the value of TD-coupling factor increases with an increasing in surrounding temperatures and these values can be fitted using a parabolic function as: $\psi(T) = 3.477 \times 10^{-7} T^2 - 1.466 \times 10^{-5} T + 8.83 \times 10^{-4}$. The similarity between the shape of TD-coupling factor curve in Figure 11 and the shape of the hysteresis loop sensitivity curve in Figure 5 (b) can be used to justify that the temperature effect can be represented by the proposed TD-coupling factor $\psi(T)$ in the proposed TD-electromechanical model. The convergence curves of the estimated parameters through the generation of the proposed algorithm are illustrated in Figure 12. Figure 12 (d) shows the convergence of the MSE $\theta(T_o)$, it can be noticed that the algorithm is saturated after 100 generations. Also, the parameters of the Maxwell-slip hysteresis model are estimated as: the dead-band width $\mathbf{d} = \{7.9475, 15.8950, 23.8425, 31.7900, 39.7375, 47.6850, 55.6325, 63.5800, 71.5275, 79.4749\}$, and the segment slopes $\mathbf{g} = \{0.3346, 0.0798, 0.0042, 0.00632, 0.0354, 0.0256, 0.0245, 0.0387, 0.0622, 0.0346\}$.

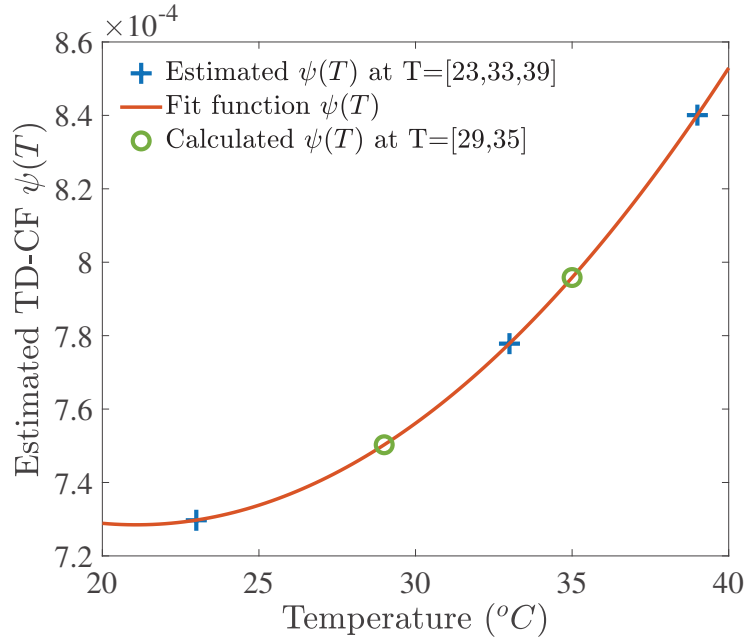


Figure 11: The estimated values of the TD-coupling factor $\psi(T)$ at different levels of surrounding temperature. The TD-coupling factor can be represented by a parabolic function as: $\psi(T) = 3.477 \times 10^{-7} T^2 - 1.466 \times 10^{-5} T + 8.83 \times 10^{-4}$.

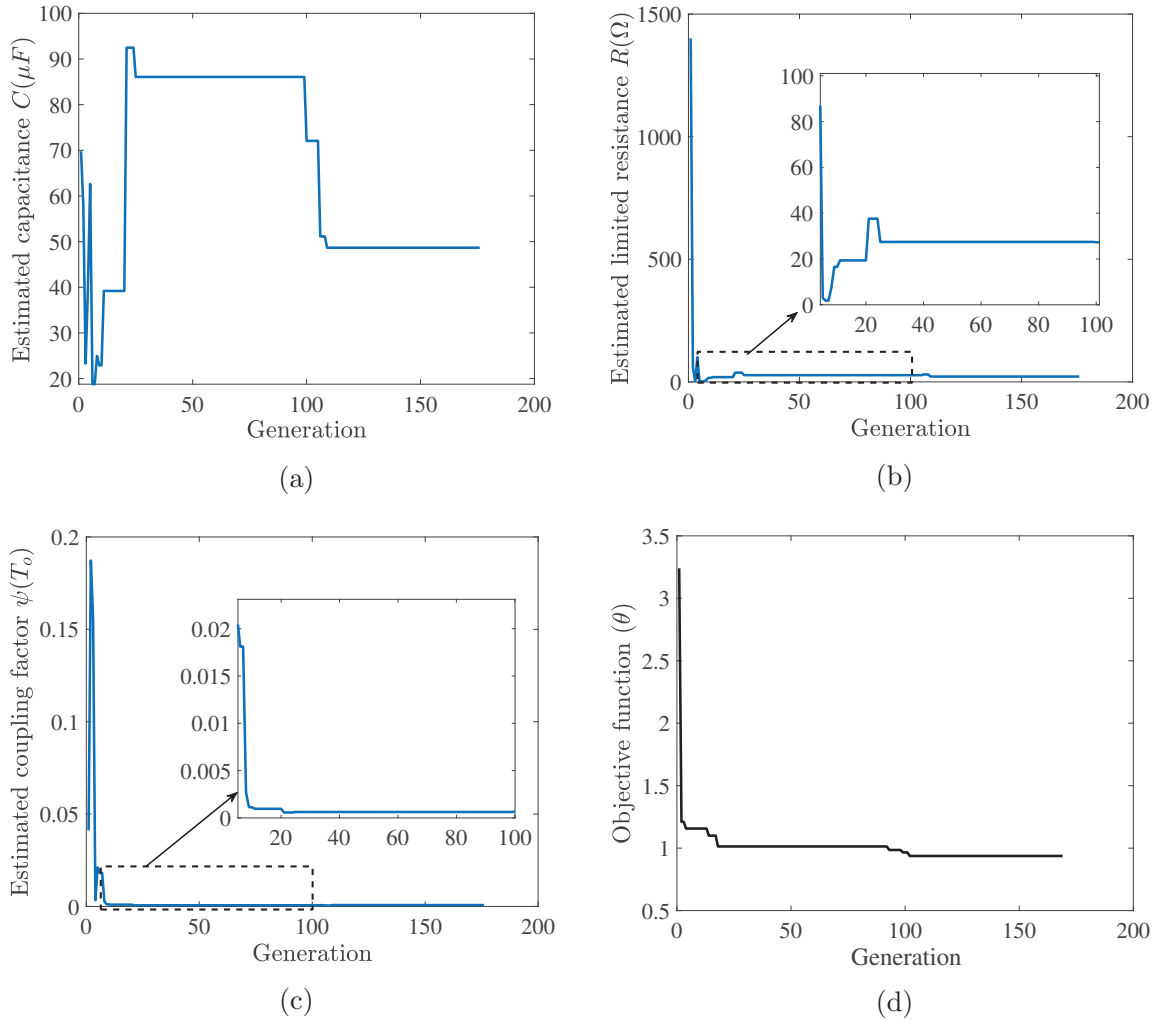


Figure 12: The convergence curve for: (a) the estimated equivalent capacitance $C(\mu F)$, (b) the estimated limited resistance $R(\Omega)$, (c) the estimated coupling factor ψ at nominal temperature $T_0 = 23^\circ C$, and (d) the Mean Square Error (MSE) $\theta(T_o) = \frac{1}{N} \sum_{k=1}^N (y[t_k] - y_E[t_k])^2$.

5.2 Parameters identification of TD-PI hysteresis model

In this work, we consider the thresholds and weights of the model are given by $r_i = \alpha i$ and $p(r_i, T_j) = \epsilon e^{\eta(T_j - T_o)} e^{-\tau r_i}$, where α , ϵ , η and τ are positive constants and $i = 0, 1, \dots, n$. In this section, the identified parameters of the TD-PI model is are represented by the vector $X = \{\alpha, \epsilon, \eta, \tau, a_0, a_1, b_1, b_2\}$. The parameters of the TD-PI model are identified through minimization

the objective function J that is given as

$$J = \min \left(\sum_{j=1}^3 \frac{1}{3} \xi(T_j) \right), \quad (30)$$

where j is the index of surrounding temperatures as $T_j = [23, 33, 39]^{\circ}C$, and $\xi(T_j)$ is the Mean Square Error (MSE) at surrounding temperature T_j given by

$$\xi(T_j) = \frac{1}{N} \sum_{k=1}^N (y(t_k) - y_{PI}(t_k))^2, \quad (31)$$

where $y(t)$ is the measured output displacement, and $y_{PI}(t)$ the output of TD-PI model at surrounding temperature T_j .

The proposed algorithm for the parameters identification of the TD-PI hysteresis model is implemented by MATLAB software based on pseudocode in [Algorithm 1](#) and [Algorithm 2](#) where different threshold numbers $n = 4, 9, \text{ and } 14$ are used. We consider 12 trials with 3000 generations at each trial. The average MSE $\xi(T_j)$ of 12 trials at different levels of surrounding temperature is illustrated in [Figure 13 \(a\)](#) which shows that increasing the threshold number n contributes decreasing in the MSE. The variation of MSE during 12 trials for threshold number $n = 9$ is illustrated using statistical box plot as shown in [Figure 13 \(b\)](#). From this figure it can be observed the small variation of MSE during 12 trials and this small variation indicates the stability of proposed algorithm for the parameters identification.

For thresholds $n = 9$, the identified parameters are $\alpha = 0.9975$, $\epsilon = 0.9770$, $\tau = 0.4167$, $\eta = 0.0091$, $a_0 = 0.0599$, $a_1 = -0.1759$, $b_0 = 0.0606$ and $b_1 = 0.2651$. Based on the identified parameters, the proposed weights $p(r_i, T_j)$ of the TD-PI model are obtained as shown in [Figure 14 \(a\)](#) where $p_0 = 0.977, 1.032, 1.089, 1.070$ and 1.130 for the surrounding temperatures $T = 23^{\circ}C, 29^{\circ}C, 33^{\circ}C, 35^{\circ}C, \text{ and } 39^{\circ}C$, respectively. [Figure 14 \(b\)](#) shows the temperature-shape function $\phi'(r_i)$ of the TD-PI model. The convergence curves of the identified parameters through the generation of the proposed algorithm are illustrated in [Figure 15](#). [Figure 15 \(d\)](#) shows that the objective function J is saturated after 1500 generations.

5.3 Simulation Results

The voltage-to-displacement hysteresis loops of the TD-electromechanical model and TD-PI model using the estimated parameters are compared with the measured hysteresis loops at different levels

Algorithm 1: The proposed algorithm for parameters identification of TD-PI hysteresis model.

```

% 1) Initialization;
G = 3000; % maximum number of generation;
S = 100; % number of candidate solutions in matrix X;
for s=1:S do
    alpha=rand; epsilon=rand; eta=rand; tau=rand;
    a0=rand; a1=rand; b0=rand; b1=rand;
    % Generate the initial generation solution matrix X1;
    X1(s, 1 : 8) = [ alpha epsilon eta tau a0 a1 b0 b1];
end
% Generate the initial values of best solutions;
Ja = 100; Xa = 0    Jb = 100; Xb = 0    Jc = 100; Xb = 0;
% 2) Start Generations of Algorithm;
for g=1:G do
    % 3) Calculate the Objective function for each solution;
    J = ObjFunc(X); % call the function ObjFunc - Algorithm 2;
    % 4) Determine the best solutions;
    Jg = sort(Jg) % sort the objective function J from lowest to highest;
    Xg = sort(Xg) % sort based on the objective function J;
    if Jg(1) ≤ Ja then
        | Ja = Jg(1); Xa = Xg(1, 1 : 8);
    end
    if Jg(2) ≤ Jb then
        | Jb = Jg(2); Xb = Xg(2, 1 : 8);
    end
    if Jg(3) ≤ Jc then
        | Jc = Jg(3); Xc = Xg(3, 1 : 8)
        | ;
    end
    % 5) Generate new solution using Equations (27), (28), and (29);
    A = 2 × a × rand - a;
    for s=1:S do
        | Da = 2 × rand × Xa - Xg(s, 1 : 8);    A1 = 2 × a × rand - a;
        | X1 = Xa - A1 × Da;
        | Db = 2 × rand × Xb - Xg(s, 1 : 8);    A2 = 2 × a × rand - a;
        | X2 = Xb - A2 × Db;
        | Dc = 2 × rand × Xc - Xg(s, 1 : 8);    A3 = 2 × a × rand - a;
        | X3 = Xc - A3 × Dc;
        | Xg+1(s, 1 : 8) = (X1 + X2 + X3)/3;
    end
    a = 2 - g × (2/G);
end
end

```

Algorithm 2: The algorithm to calculate the objective function of Algorithm 1.

```

function  $J = \text{ObjFunc}(X)$ ;
 $S = 100$ ; % number of candidate solutions in matrix  $X$ ;
 $n = 9$ ; % threshold numbers;
 $N =$ ; % number of sample;
 $T = [23 \ 33 \ 39]$ ;  $T_0 = 23$ ;
% Tested temperature;
for  $s=1:S$  do
    % get the candidate paramters;
     $\alpha = X^g(s, 1)$ ;  $\epsilon = X^g(s, 2)$ ;  $\eta = X^g(s, 3)$ ;  $\tau = X^g(s, 4)$ ;
     $a_0 = X^g(s, 5)$ ;  $a_1 = X^g(s, 6)$ ;  $b_0 = X^g(s, 7)$ ;  $b_1 = X^g(s, 8)$ ;
    for  $j=1:3$  do
         $J_s = 0$  % variable for sum objective function  $J$ ;
        % calculate the thresholds and the weights;
        for  $i=1:n+1$  do
             $r(i) = \alpha * (i - 1)$ ;
             $p(i) = \epsilon * \exp(-\tau * r(i)) * \exp(\eta * (T(j) - T_0))$ ;
        end
        for  $k=2:N$  do
             $pF_r = 0$  % variable for sum playoperator;
             $E = 0$  % variable for sum Error;
            for  $i=2:n+1$  do
                % calculate the output of playoperator using Equation (24);
                 $F_r(t_1) = 0$ ;
                 $\gamma_l = a_0 * v_s(t_k) + a_1$ ;
                 $\gamma_r = b_0 * v_s(t_k) + b_1$ ;
                 $F_r(t_k) = \max(\gamma_l - r(i), \min(\gamma_r + r(i), Fr(i, t_{k-1})))$ ;
                 $S1 = S1 + p(i) * F_r(t_k)$ ;
            end
            % calculate the output of TD-PI model using Equation (25);
             $y_{PI}(t_k) = p(1) * v_s(t_k) + S1$ ;
             $E = E + (y(t_k) - y_{PI}(t_k))^2$ ;
        end
         $\xi(j) = 1/N * E$ ; % calculate the MSE;
         $J_s = J_s + \xi(j)$ ;
    end
     $J(s) = 1/3 * J_s$ ; % calculate the objective function  $J$  for solution  $s$ ;
end

```

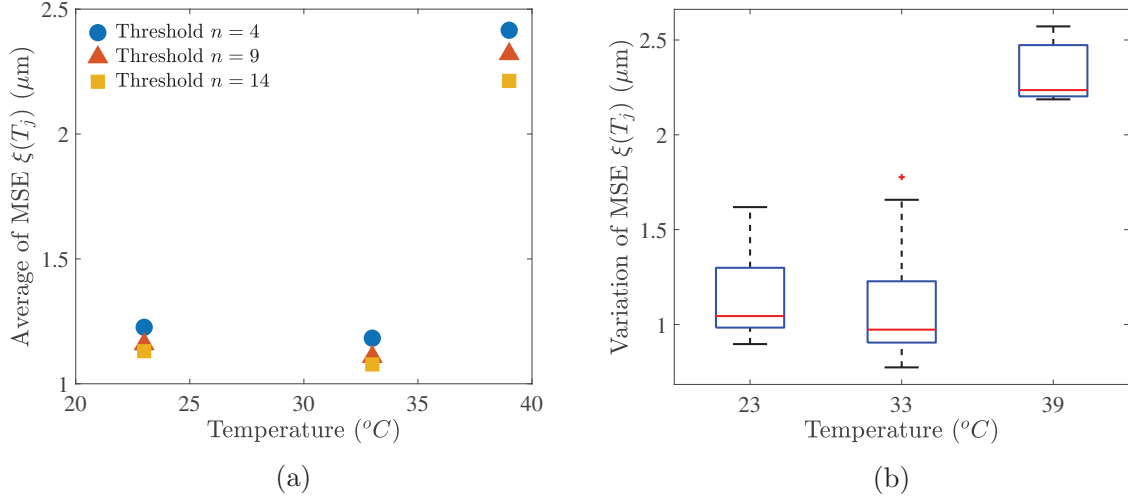


Figure 13: (a) Average of MSE for 12 trials using different thresholds number $n = 4, 9,$ and 14 at different levels of surrounding temperatures, and (b) Statistical box plot representation of the variation of MSE for 12 trials using threshold number $n = 9$.

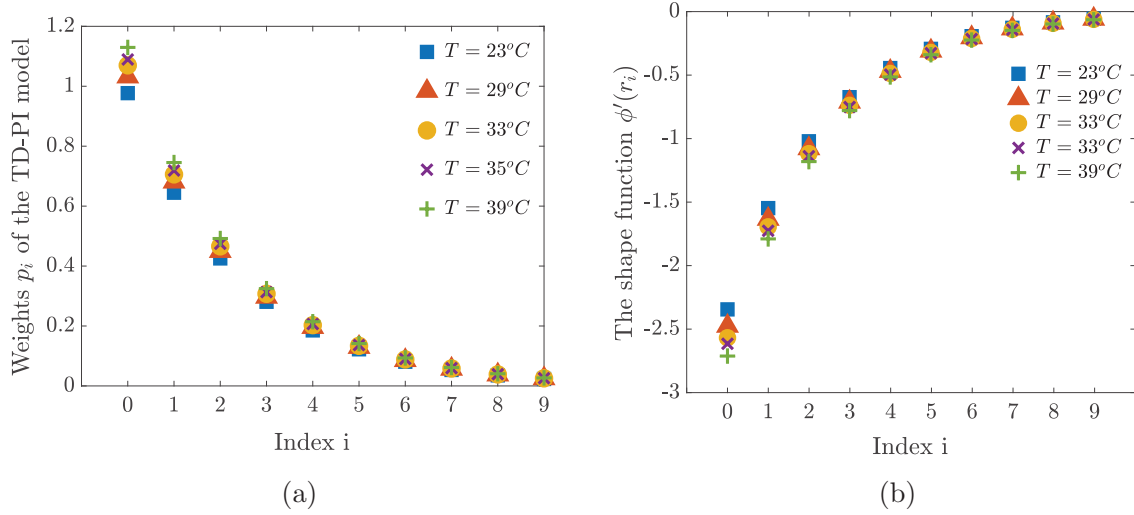


Figure 14: (a) The proposed weights $p(r_i, T_j)$ of TD-PI model at different levels of surrounding temperature, and (b) The temperature-shape function $\phi'(r_i)$.

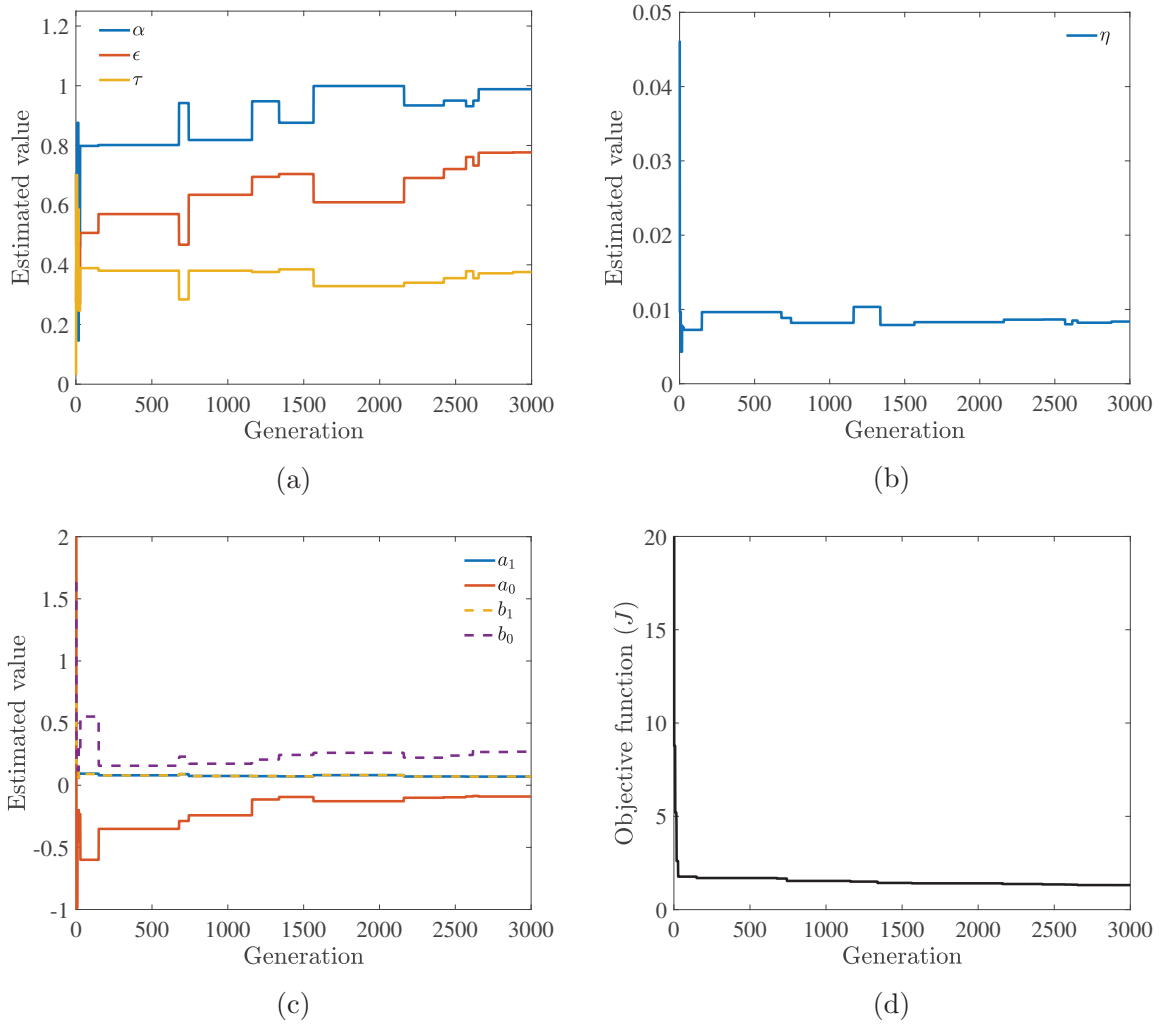


Figure 15: The convergence curve for: (a) the estimated parameters α , ρ , and τ , (b) the estimated parameter η , (c) the estimated parameters a_0 , a_1 , b_0 , and b_1 , and (d) the objective function $J = \min \left(\sum_{j=1}^3 \frac{1}{3} \xi(T_j) \right)$.

of surrounding temperatures as shown in Figure 16. As the figure illustrates, the two proposed models well approximate the temperature-dependent hysteresis nonlinearities of piezoelectric tube actuator. Similar to the experimental observation, the estimated hysteresis loops for the TD-electromechanical model and the TD-PI model in Figure 17 (a) and (b) show that increasing the surrounding temperature yields an increase in the sensitivity (mean slope). Also, two models show an increase in the sensitivity with the surrounding temperature as depicted in Figure 17 (c) and (d).

Figure 18 shows the modeling errors as the difference between the measured output displacement and the output of two proposed models as a function of time at different levels of surrounding temperatures. It indicates that the error of two proposed models are bounded between $[-2\mu m, 2\mu m]$ and this is accepted for the measured output displacement of $[-30\mu m, 30\mu m]$. Comparison between the TD-electromechanical model and the TD-PI model is carried through calculating the Mean Square Error (MSE) and the Maximum Absolute Error (MAE) as illustrated using the bar plot in Figure 19 (a) and (b), respectively.

6 The Inverse Temperature-Dependent Prandtl-Ishlinskii (TD-PI) Model

In the section, we derive the inverse TD-PI model analytically. The objective is to propose the inverse model that acts as a feedforward compensator to reduce temperature effects on the hysteresis nonlinearities of the piezoelectric actuators without using feedback sensors. Analytically, the output of the compensation when the inverse TD-PI is used should yield

$$\mathcal{P} \circ \mathcal{Q}[y_d](t) = y_d(t), \quad (32)$$

where $\mathcal{Q} = \mathcal{P}^{-1}$ is the output of the inverse TD-PI model and $y_d(t)$ is the input desired displacement.

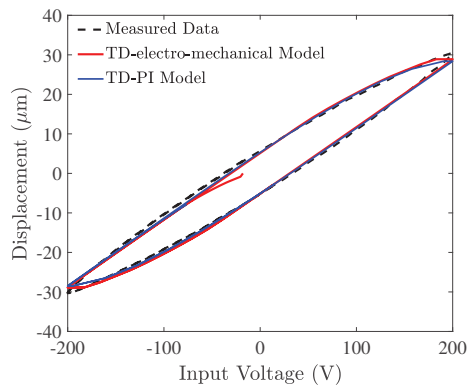
6.1 Formulation of the inverse TD-PI hysteresis model

The temperature shape function that was presented in the Section 4.2 can be used to calculate the inverse TD-PI model \mathcal{P}^{-1} with the initial loading curve. We define the output of the inverse model as

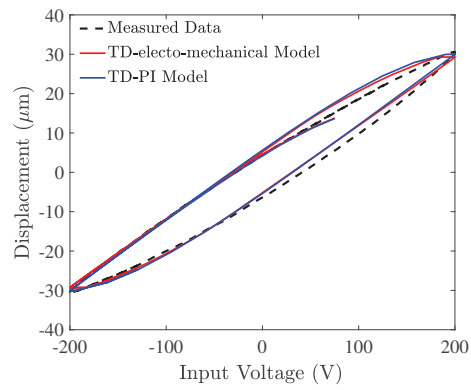
$$\mathcal{Q}[y_d, \bar{T}](t) = \int_0^Z q(z, \bar{T}) \mathcal{F}_z[y_d](t) dz, \quad (33)$$

$q(z, \bar{T})$ is an integrable weight function of threshold z with $q(z, \bar{T}) = 0$ for $z > Z$ where Z is a positive constant that is determined by the experimental results and the desired output. In order to obtain the inverse model, we need to identify the density function $q(z, \bar{T})$ and the threshold values z considering the density function $p(r, \bar{T})$ and the thresholds r .

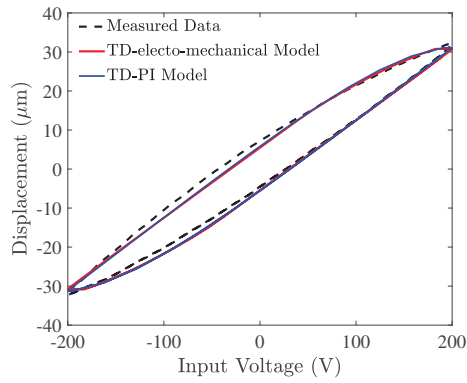
For a positive threshold z and a shape function ψ , the inverse TD-PI model $\mathcal{P}^{-1}[y_d](t)$ is



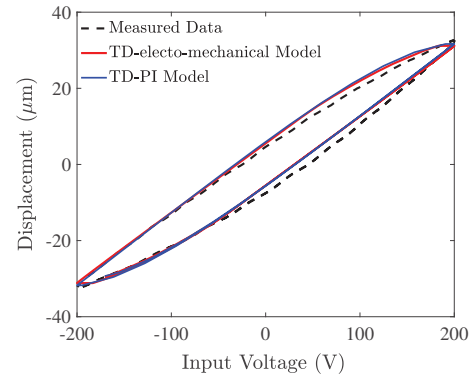
(a)



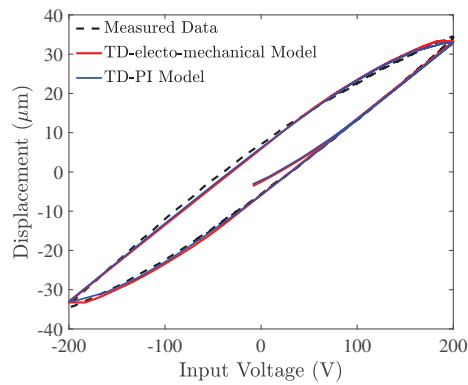
(b)



(c)

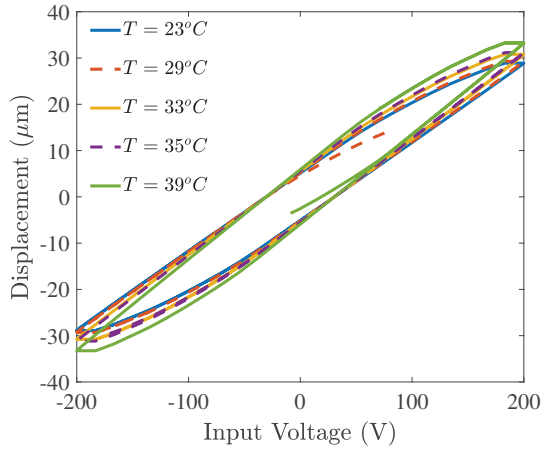


(d)

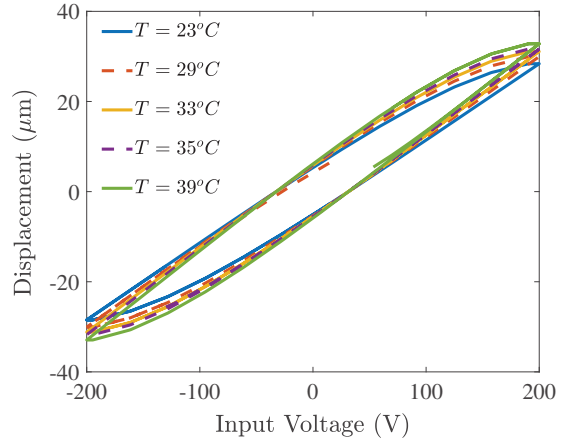


(e)

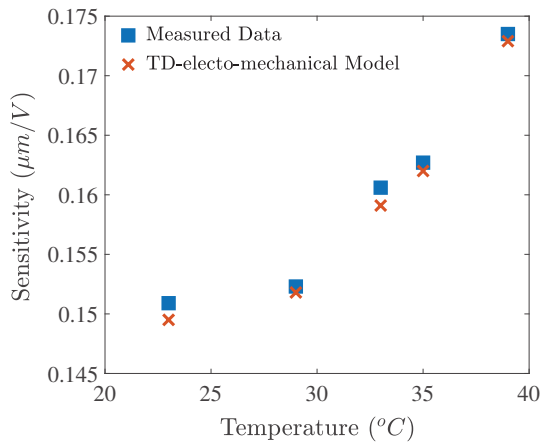
Figure 16: Comparison between the measured voltage-to-displacement hysteresis loops and the estimated voltage-to-displacement hysteresis loops using the TD-electromechanical model and the TD-PI model at surrounding temperatures of (a) $T = 23^{\circ}C$, (b) $T = 29^{\circ}C$, (c) $T = 33^{\circ}C$, (d) $T = 35^{\circ}C$, and (e) $T = 39^{\circ}C$.



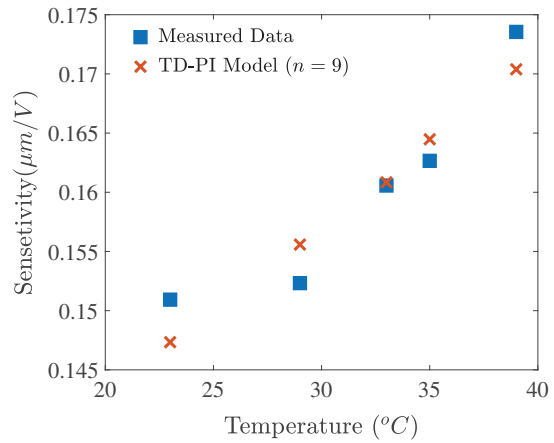
(a)



(b)

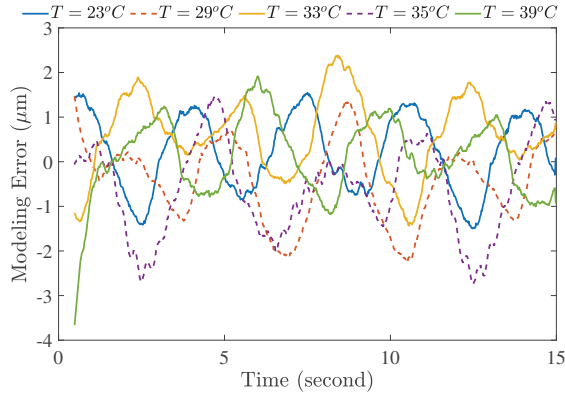


(c)

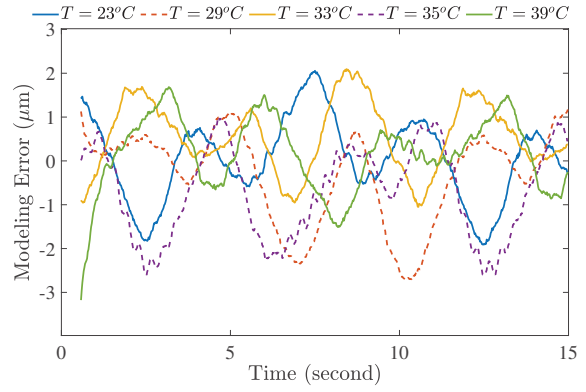


(d)

Figure 17: The voltage-to-displacement hysteresis loops at different surrounding temperatures of $T = 23^{\circ}C$, $29^{\circ}C$, $33^{\circ}C$, $35^{\circ}C$ and $39^{\circ}C$ using:(a) the TD-electromechanical model, and (b) the TD-PI model. The calculated sensitivity compared with the measured data for the piezoelectric tube actuator at surrounding temperatures of $T = 23^{\circ}C$, $29^{\circ}C$, $33^{\circ}C$, $35^{\circ}C$, and $39^{\circ}C$ using: (c) the TD-electromechanical model and (d) the TD-PI model.

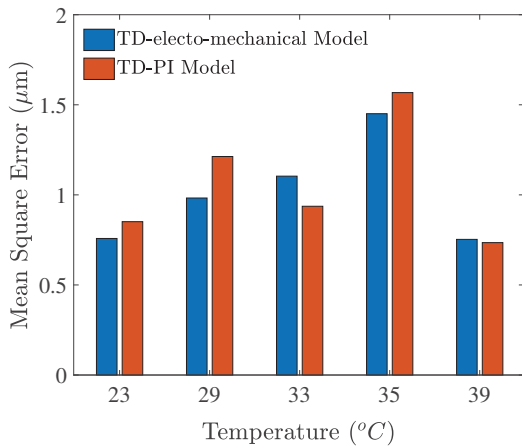


(a)

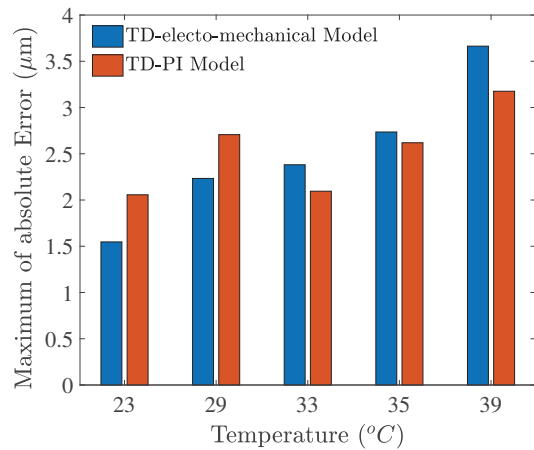


(b)

Figure 18: The history of error signals between the measured output displacement and the estimated output displacement at surrounding temperatures of $T = 23^\circ\text{C}$, 29°C , 33°C , 35°C , and 39°C using: (a) the TD-electromechanical model, and (b) the TD-PI model.



(a)



(b)

Figure 19: Comparison between the TD-electromechanical model and the TD-PI mode at different surrounding temperatures of $T = 23^\circ\text{C}$, 29°C , 33°C , 35°C , and 39°C using the calculated: (a) Mean Square Error (MSE), and (b) Maximum Absolute Error (MAE).

expressed as

$$\mathcal{P}^{-1}[y_d](t) = q_0 y_d(t) + \int_0^Z q(T) \psi_z''(z) \mathcal{F}_z[y_d](t) dz, \quad (34)$$

where

$$\psi(z, \bar{T}) = q_0 z + \int_0^z q(\tau, \bar{T})(z - \tau) d\tau \quad (35)$$

and

$$\psi(z, \bar{T}) = q_0 z + q_T(\bar{T}) \int_0^z q_z(\tau_z)(z - \tau_z) d\tau_z. \quad (36)$$

Then, at any surrounding temperature T

$$\psi_z \circ \phi_r(r, \bar{T}) = r, \quad (37)$$

where ϕ and ψ are the temperature shape function and its inverse, respectively. Equation (37) can be derived with respect to the threshold r and z to obtain the slope of the temperature hysteresis model and its inverse. Consequently:

$$\frac{\partial}{\partial r} (\psi \circ \phi(r, \bar{T}) = r) \quad (38)$$

and

$$p_T(\bar{T}) \phi_r' q_T(\bar{T}) \psi_z'(\phi_r(r)) = 1. \quad (39)$$

We can conclude

$$z = \phi(r).$$

Then, the exact inverse of temperature hysteresis model can be obtained using the temperature-shape function and Equation (39).

6.2 The inverse discrete TD-PI hysteresis model

The discrete form of inverse TD-PI model is presented in this section on the basis of the continuous form that was presented in the previous section. The output of the inverse model is

$$v_s(t) = \mathcal{P}_T^{-1}[y_d](t) = q_0 y_d(t) + q_T(\bar{T}) \sum_{i=1}^n q_z(z_i) \mathcal{F}_{z_i}[y_d](t). \quad (40)$$

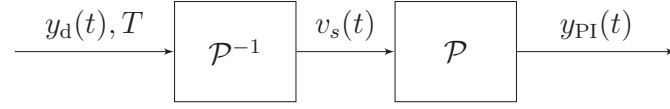


Figure 20: Block diagram representation of open-loop feedforward compensation using the inverse TD-PI model, \mathcal{P}^{-1} is the inverse TD-PI model, \mathcal{P} is the TD-PI model, $y_d(t)$ is the input desired displacement, T is the measured surrounding temperature, $v_s(t)$ is the output of the inverse TD-PI model, and $y_{PI}(t)$ is the output of the TD-PI model.

For each interval $r \in [r_i, r_{i+1})$ and $z \in [z_i, z_{i+1})$, we have

$$q_T(\bar{T}_j)\psi'_z(z) = \frac{1}{p_T(\bar{T}_j)\phi'_r}. \quad (41)$$

This implies we completely compensate the effects of the hysteresis at any temperature T . Let $q_i = q(z_i)$ and $p_i = p(r_i)$ and for any threshold interval, we have for $i = 1, 2, \dots, n$

$$q_0 + q_T(\bar{T}_j) \sum_{i=1}^n q_i = \frac{1}{p_0 + p_T(\bar{T}_j) \sum_{i=1}^n p_i}, \quad (42)$$

and the thresholds of the inverse TD-PI model is obtained with

$$z_j - z_{j-1} = p_0 + \sum_{i=1}^{j-1} p_T(\bar{T}_j)p_i(r_j - r_{j-1}). \quad (43)$$

Then, the inverse TD-PI can be used as a feedforward compensator to reduce the hysteresis effects at different level of temperatures.

6.3 Simulation results for feedforward compensation

The inverse TD-PI model is applied for compensation of hysteresis nonlinearities of the TD-PI model in open-loop feedforward manner as representing by the block diagram in [Figure 20](#).

For thresholds $n = 9$, the identified parameters are $\alpha = 0.9975$, $\epsilon = 0.9770$, $\tau = 0.4167$ and $\eta = 0.0091$, $p_0 = 0.977, 1.032, 1.089, 1.070$ and 1.130 for the surrounding temperatures $T = 23^\circ C, 29^\circ C, 33^\circ C, 35^\circ C,$ and $39^\circ C$, respectively. The identified coefficients of envelope functions are $a_0 = 0.0599$, $a_1 = -0.1759$, $b_0 = 0.0606$ and $b_1 = 0.2651$. Based on the identified parameters, the calculated thresholds z_i and weights q_i of the inverse TD-PI model are obtained as shown in [Figure 21](#). The simulations are carried out to explore the performance of the proposed inverse model in compensating of hysteresis over different temperatures. [Figure 22](#) illustrates the

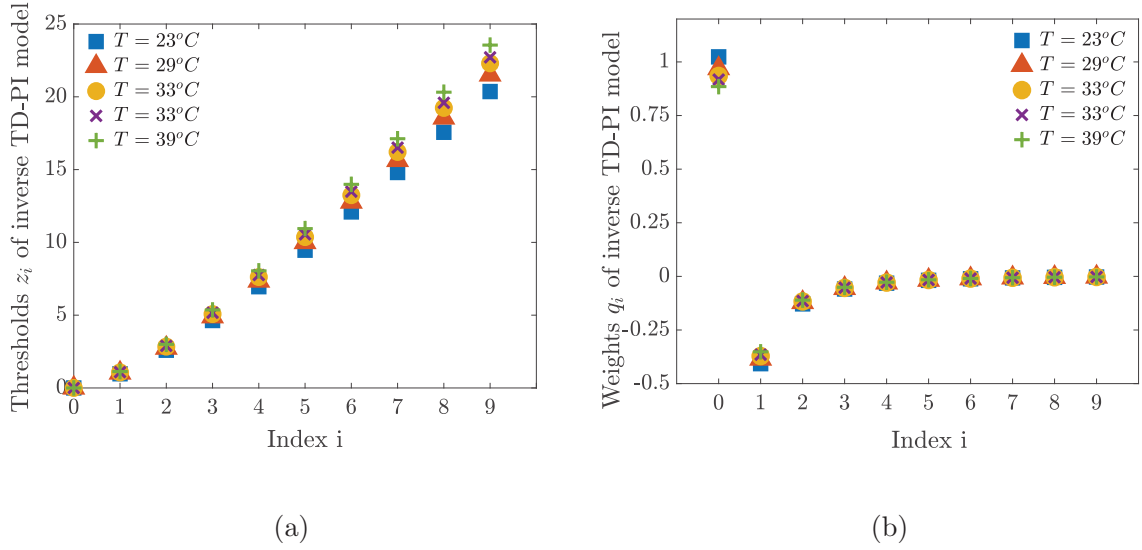


Figure 21: (a) The calculated thresholds z_i of the inverse TD-PI hysteresis model, and (b) The calculated weights q_i of the inverse TD-PI hysteresis model.

displacement-to-voltage characteristic of the inverse TD-PI model due to a desired input displacement $y_d(t) = 30 \sin(2\pi ft) \mu m$ of frequency $f = 0.1$ Hz at different input surrounding temperatures of $T = 23^\circ C$, $29^\circ C$, $33^\circ C$, $35^\circ C$, and $39^\circ C$. Figure 23 displays the output of inverse compensation versus the desired input displacement. The figure shows that the inverse TD-PI model can completely compensate the hysteresis nonlinearities of the TD-PI model at different levels of surrounding temperatures.

7 Conclusion and Future work

Modeling the hysteresis nonlinearities of piezoelectric material-based actuators has attracted a lot of attention from researchers in last years. The proposed hysteresis models that relate the voltage-to-displacement behavior are valid under different input voltage amplitudes, excitation frequencies, input voltage biases, and stress levels. However, the extension of these models to consider surrounding temperature effects is proposed in few works.

An experimental study was used to measure the voltage-to-displacement hysteresis nonlinearities loops of piezoelectric tube actuator under different surrounding temperatures. The output displacement of a piezoelectric tube actuator that exhibits hysteresis was characterized under different surrounding temperatures and the measured hysteresis loops demonstrated that increasing the temperature contributes an increase in the sensitivity of the actuator displacement within the

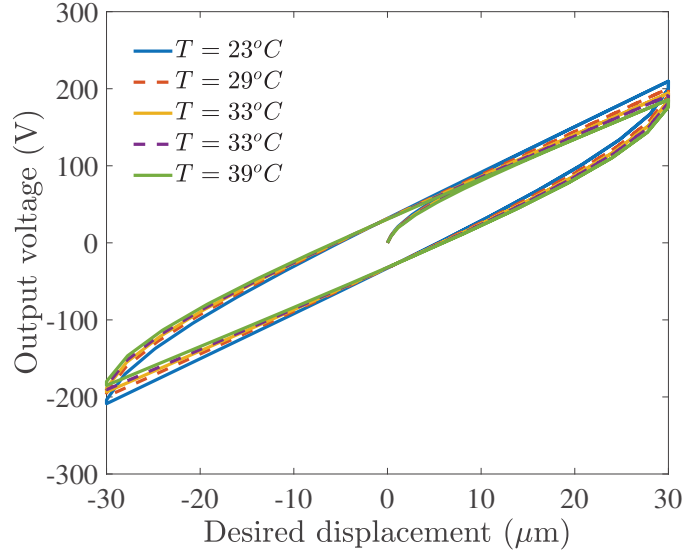
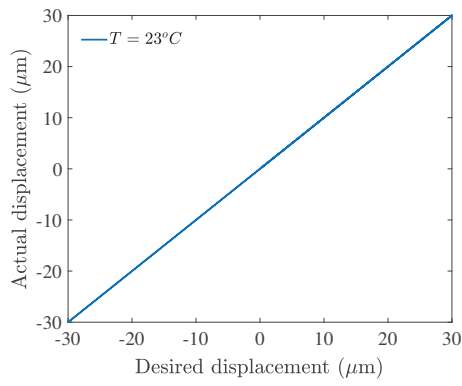


Figure 22: The displacement-to-voltage characteristic of the inverse TD-PI model due to a desired input displacement $y_d(t) = 30 \sin(2\pi ft)$ V of frequency $f = 0.1$ Hz at different input surrounding temperatures of $T = 23^\circ C$, $29^\circ C$, $33^\circ C$, $35^\circ C$, and $39^\circ C$.

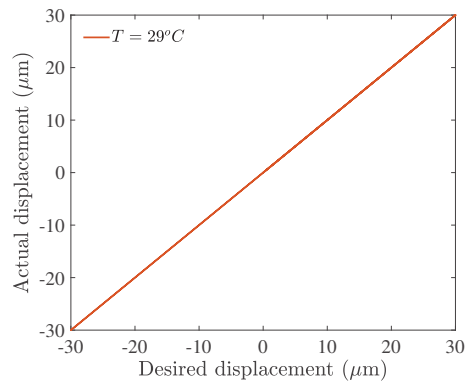
operating range that was considered in the experimental study.

Then, two temperature-dependent models were proposed to account the hysteresis nonlinearities under the effect of the surrounding temperatures. The first model is the Temperature-dependent electromechanical model that is presented to describe the electrical and mechanical properties of the piezoelectric tube actuator using electrical and mechanical elements with the proposed temperature-dependent coupling factor. The mathematical formulation of this model was obtained, and then the physical simulation model implemented using Simscape library in MATLAB-simulink software was used to simulate and estimate the output of the proposed TD-electromechanical model. The second model is Temperature-dependent Prandtl-Ishlinskii that is derived based on the proposed temperature shape function to characterize the voltage-to-displacement hysteresis nonlinearities of the piezoelectric tube actuator. The parameters of the two proposed models were obtained using proposed optimization algorithms based on Grey Wolf Optimizer.

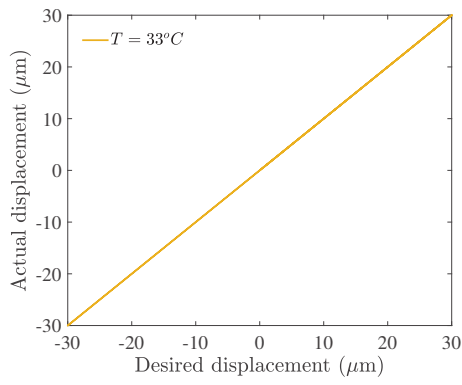
The obtained simulation results show that the two proposed models can be account for characterization of the hysteresis nonlinearities under different surrounding temperatures. The estimated output displacement obtained using two proposed model show that increasing the different surrounding temperatures yields an increase in the sensitivity of the hysteresis loops. The comparison between the measured hysteresis loops and the estimated hysteresis loops of two proposed mod-



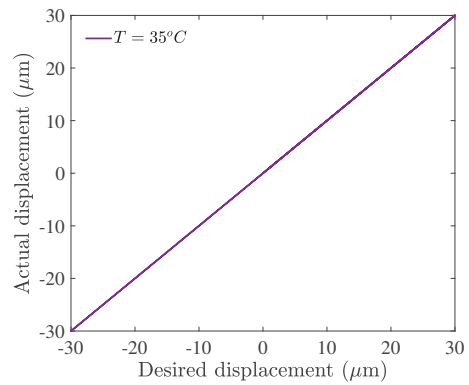
(a)



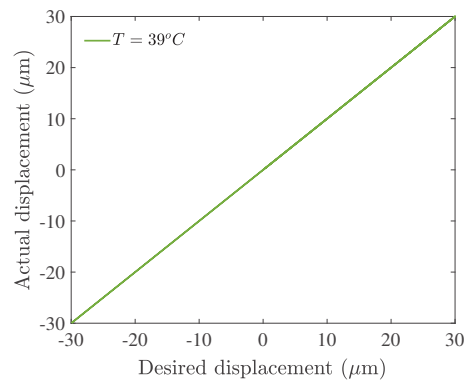
(b)



(c)



(d)



(e)

Figure 23: Feedforward compensation results for a desired input displacement $y_d(t) = 30 \sin(2\pi ft)$ V of frequency $f = 0.1$ Hz at different input surrounding temperatures of: (a) $T = 23^\circ\text{C}$, (b) $T = 29^\circ\text{C}$, (c) $T = 33^\circ\text{C}$, (d) $T = 35^\circ\text{C}$, and (e) $T = 39^\circ\text{C}$.

els indicates that the modeling error of two proposed models is bounded between $[-2\mu m, 2\mu m]$ which is accepted for the entire range of displacement $[-30\mu m, 30\mu m]$ which it show the ability of two proposed models to describe the hysteresis nonlinearities under the different levels of surrounding temperatures that were imposed to the piezoelectric tube actuator. Two criteria, the mean square error and maximum absolute error, indicate there minimum difference between two proposed models.

The modeling results were followed by formulating of an inverse TD-PI model that can be compensate for the hysteresis nonlinearities of the model. The inverse compensator was applied afterwards for compensation of hysteresis nonlinearities of the TD-PI model in open-loop manner. The simulation results showed that the inverse TD-PI model can cancel out the temperature-dependent hysteresis properties of the piezoelectric tube actuator. In applications, the proposed models can be used to design control systems to reduce the hysteresis effects of the piezoelectric tube scanners for scanning and positioning in Atomic Force Microscopes (AMF). The results of this study will be extended in the future work to include modeling and experimental compensation the displacements along multi-axis, and when the frequency of the harmonic input voltage is also varied, additionally to the temperature variation.

Acknowledgement

This work was supported by the Natural Sciences and Engineering Research Council of Canada and Mobility funding for researchers (French Embassy in Canada).

References

- [1] R. C. Smith, *Smart Material Systems: Model Development*. Society for Industrial Applied Mathematics, United States, 2005.
- [2] J. Crews, N. Bravo, and R. Smith, "Model Development for PZT Bimorph Actuation Employed for Micro-air Vehicles," in *ASME 2016 Conference on Smart Materials, Adaptive Structures and Intelligent Systems*, pp. 1–6, 2016.
- [3] Y. Tian, K. Cai, D. Zhang, X. Liu, F. Wang, and B. Shirinzadeh, "Development of a XYZ Scanner for Home-made Atomic Force Microscope Based on FPAA Control," *Mechanical Systems and Signal Processing*, vol. 131, pp. 222–242, 2019.

- [4] P. Liu, P. Yan, and H. Özbay, “Design and Trajectory Tracking Control of a Piezoelectric Nano-manipulator with Actuator Saturations,” *Mechanical Systems and Signal Processing*, vol. 111, pp. 529–544, 2018.
- [5] Z.-c. Qiu, B. Wang, X.-m. Zhang, and J.-d. Han, “Direct Adaptive Fuzzy Control of a Translating Piezoelectric Flexible Manipulator Driven by a Pneumatic Rodless cylinder,” *Mechanical Systems and Signal Processing*, vol. 36, no. 2, pp. 290–316, 2013.
- [6] Y.-J. Li, J. Zhang, Z.-Y. Jia, and M. Qian, “A Novel Piezoelectric 6-Component Heavy Force/moment Sensor for Huge Heavy-load Manipulator’s Gripper,” *Mechanical Systems and Signal Processing*, vol. 23, no. 5, pp. 1644–1651, 2009.
- [7] F. Stefanski, B. Minorowicz, J. Persson, A. Plummer, and C. Bowen, “Non-linear Control of a Hydraulic Piezo-valve Using a Generalised Prandtl–Ishlinskii hysteresis Model,” *Mechanical Systems and Signal Processing*, vol. 82, pp. 412–431, 2017.
- [8] F. J. Salvador, A. H. Plazas, J. Gimeno, and M. Carreres, “Complete Modelling of a Piezo Actuator Last-generation Injector for Diesel Injection Systems,” *International Journal of Engine Research*, vol. 15, no. 1, pp. 3–19, 2014.
- [9] S. Lescano, M. Rakotondrabe, and N. Andreff, “Precision Prediction Using Interval Exponential Mapping of a Parallel Kinematic Smart Composite Microstructure,” in *International Conference on Intelligent Robots and Systems*, pp. 1994–1999, 2015.
- [10] P. Li, F. Yan, C. Ge, X. Wang, L. Xu, J. Guo, and P. Li, “A Simple Fuzzy System for Modelling of Both Rate-independent and Rate-dependent Hysteresis in Piezoelectric Actuators,” *Mechanical Systems and Signal Processing*, vol. 36, no. 1, pp. 182–192, 2013.
- [11] A. Milecki and M. Pelic, “Application of Geometry Based Hysteresis Modelling in Compensation of Hysteresis of Piezo Bender Actuator,” *Mechanical Systems and Signal Processing*, vol. 78, pp. 4–17, 2016.
- [12] L. Liu, Y. Zhao, L. Tang, Y. Xu, Y.-g. Bai, and H. Liao, “Modeling and Identification Investigation of Multi-field Hysteretic Dynamics in Flexure-guided Piezo Platform,” *Mechanical Systems and Signal Processing*, vol. 50, pp. 594–606, 2015.
- [13] S. Shao, M. Xu, S. Zhang, and S. Xie, “Stroke Maximizing and High Efficient Hysteresis Hybrid Modeling for a Rhombic Piezoelectric Actuator,” *Mechanical Systems and Signal Processing*, vol. 75, pp. 631–647, 2016.

- [14] Z. Zhu, S. To, Y. Li, W.-L. Zhu, and L. Bian, “External Force Estimation of a Piezo-actuated Compliant Mechanism Based on a Fractional Order Hysteresis Model,” *Mechanical Systems and Signal Processing*, vol. 110, pp. 296–306, 2018.
- [15] D. Habineza, M. Zouari, Y. L. Gorrec, and M. Rakotondrabe, “Characterization and Modeling of the Temperature Effect on The Piezoelectric Tube Actuator,” in *Symposium on Mechatronic Systems*, pp. 354–360, 2016.
- [16] G. Aguirre, T. Janssens, H. Van Brussel, and F. Al-Bender, “Asymmetric-hysteresis Compensation in Piezoelectric Actuators,” *Mechanical Systems and Signal Processing*, vol. 30, pp. 218–231, 2012.
- [17] Z. Sun, B. Song, N. Xi, R. Yang, L. Hao, Y. Yang, and L. Chen, “Asymmetric Hysteresis Modeling and Compensation Approach for Nanomanipulation System Motion Control Considering Working-range Effect,” *IEEE Transactions on Industrial Electronics*, vol. 64, no. 7, pp. 5513–5523, 2017.
- [18] Q. Zhang, Y. Dong, Y. Peng, J. Luo, S. Xie, and H. Pu, “Asymmetric Bouc–Wen Hysteresis Modeling and Inverse Compensation for Piezoelectric Actuator via a Genetic Algorithm–based Particle Swarm Optimization Identification Algorithm,” *Journal of Intelligent Material Systems and Structures*, vol. 30, no. 8, pp. 1263–1275, 2019.
- [19] S. Yi, B. Yang, and G. Meng, “Microvibration Isolation by Adaptive Feedforward Control with Asymmetric Hysteresis Compensation,” *Mechanical Systems and Signal Processing*, vol. 114, pp. 644–657, 2019.
- [20] M. Al Janaideh and P. Krejčí, “Inverse Rate-dependent Prandtl–Ishlinskii Model for Feedforward Compensation of Hysteresis in a Piezomicropositioning Actuator,” *IEEE/ASME Transactions on Mechatronics*, vol. 18, no. 5, pp. 1498–1507, 2012.
- [21] O. Aljanaideh, M. Al Janaideh, and M. Rakotondrabe, “Inversion-free Feedforward Dynamic Compensation of Hysteresis Nonlinearities in Piezoelectric Micro/nano-positioning Actuators,” in *IEEE International Conference on Robotics and Automation*, pp. 2673–2678, 2015.
- [22] K. Li, Z. Yang, M. Lallart, S. Zhou, Y. Chen, and H. Liu, “Hybrid Hysteresis Modeling and Inverse Model Compensation of Piezoelectric Actuators,” *Smart Materials and Structures*, vol. 28, no. 11, pp. 1–15, 2019.

- [23] Y.-D. Tao, H.-X. Li, and L.-M. Zhu, “Rate-dependent Hysteresis Modeling and Compensation of Piezoelectric Actuators Using Gaussian Process,” *Sensors and Actuators A: Physical*, vol. 295, pp. 357–365, 2019.
- [24] Y. Wu, Y. Fang, C. Liu, Z. Fan, and C. Wang, “Gated Recurrent Unit Based Frequency-dependent Hysteresis Modeling and End-to-end Compensation,” *Mechanical Systems and Signal Processing*, vol. 136, pp. 1–19, 2020.
- [25] M. Stuebner, J. Atulasimha, and R. Smith, “Quantification of Hysteresis and Nonlinear Effects on The Frequency Response of Ferroelectric and Ferromagnetic Materials,” *Smart Materials and Structures*, vol. 18, no. 10, pp. 1–10, 2009.
- [26] O. Aljanaideh, M. D. Al-Tahat, and M. Al Janaideh, “Rate-bias-dependent Hysteresis Modeling of A Magnetostrictive Transducer,” *Microsystem Technologies*, vol. 22, no. 4, pp. 883–892, 2016.
- [27] W. Zhu, L. X. Bian, L. Cheng, and X. T. Rui, “Non-linear Compensation and Displacement Control of The Bias-rate-dependent Hysteresis of a Magnetostrictive Actuator,” *Precision Engineering*, vol. 50, pp. 107–113, 2017.
- [28] V. Apicella, C. S. Clemente, D. Davino, D. Leone, and C. Visone, “Self-sensing Estimation of Mechanical Stress in Magnetostrictive Actuators,” *IEEE Transactions on Magnetics*, vol. 55, no. 1, pp. 1–5, 2018.
- [29] O. Aljanaideh, M. Miyasaka, and B. Hannaford, “Integrated Asymmetric Stop Operator Based Model for Strain Stress Hysteresis Characteristics of Cable Driven Robots Loaded Longitudinally,” in *IEEE/RSJ International Conference on Intelligent Robots and Systems*, pp. 2543–2548, 2017.
- [30] V. Hassani, T. Tjahjowidodo, and T. N. Do, “A Survey on Hysteresis Modeling, Identification and Control,” *Mechanical Systems and Signal Processing*, vol. 49, no. 1-2, pp. 209–233, 2014.
- [31] J. Gan and X. Zhang, “A Review of Nonlinear Hysteresis Modeling and Control of Piezoelectric Actuators,” *AIP Advances*, vol. 9, no. 4, pp. 1–10, 2019.
- [32] M. Goldfarb and N. Celanovic, “Modeling Piezoelectric Stack Actuators for Control of Micromanipulation,” *IEEE Control Systems*, vol. 17, no. 3, pp. 69–79, 1997.
- [33] H. Adriaens, W. L. De Koning, and R. Banning, “Modeling Piezoelectric Actuators,” *IEEE/ASME Transactions on Mechatronics*, vol. 5, no. 4, pp. 331–341, 2000.

- [34] H. Saoulli and R. B. Mrad, "Modeling Piezoceramic Actuators for Smart Applications," *IFAC Proceedings Volumes*, vol. 35, no. 2, pp. 155–160, 2002.
- [35] H. M. Georgiou and R. B. Mrad, "Electromechanical Modeling of Piezoceramic Actuators for Dynamic Loading Applications," *Journal of Dynamic Systems, Measurement, and Control*, vol. 128, no. 3, pp. 558–567, 2006.
- [36] H. Georgiou and R. B. Mrad, "Dynamic Electromechanical Drift Model for PZT," *Mechatronics*, vol. 18, no. 2, pp. 81–89, 2008.
- [37] M. Quant, H. Elizalde, A. Flores, R. Ramírez, P. Orta, and G. Song, "A Comprehensive Model for Piezoceramic Actuators: Modelling, Validation and Application," *Smart Materials and Structures*, vol. 18, no. 12, pp. 1–16, 2009.
- [38] L. Juhász, J. Maas, and B. Borovac, "Parameter Identification and Hysteresis Compensation of Embedded Piezoelectric Stack Actuators," *Mechatronics*, vol. 21, no. 1, pp. 329–338, 2011.
- [39] M. N. Islam and R. J. Seethaler, "An Improved Electromechanical Model and Parameter Identification Technique for Piezoelectric Actuators," *Journal of Intelligent Material Systems and Structures*, vol. 24, no. 9, pp. 1049–1058, 2013.
- [40] J. Liu, W. J. O'Connor, E. Ahearne, and G. Byrne, "Electromechanical Modelling for Piezoelectric Flexensional Actuators," *Smart Materials and Structures*, vol. 23, no. 2, pp. 1–13, 2013.
- [41] L. Prandtl, "Ein Gedankenmodell Zur Kinetischen Theorie Der Festen Körper," *ZAMM—Journal of Applied Mathematics and Mechanics Zeitschrift für Angewandte Mathematik und Mechanik*, vol. 8, no. 2, pp. 85–106, 1928.
- [42] M. Al Janaideh, S. Rakheja, and C.-Y. Su, "A Generalized Prandtl–Ishlinskii Model for Characterizing The Hysteresis and Saturation Nonlinearities of Smart Actuators," *Smart Materials and Structures*, vol. 18, no. 4, pp. 1–9, 2009.
- [43] P. Krejci and K. Kuhnen, "Inverse Control of Systems with Hysteresis and Creep," *IEE Proceedings—Control Theory and Applications*, vol. 148, no. 3, pp. 185–192, 2001.
- [44] M. Al Janaideh, S. Rakheja, and C.-Y. Su, "An Analytical Generalized Prandtl–Ishlinskii Model Inversion for Hysteresis Compensation in Micropositioning Control," *IEEE/ASME Transactions on Mechatronics*, vol. 16, no. 4, pp. 734–744, 2011.

- [45] M. Al Janaideh and P. Krejčí, “Inverse Rate-dependent Prandtl–Ishlinskii Model for Feedforward Compensation of Hysteresis in a Piezomicropositioning Actuator,” *IEEE/ASME Transactions on Mechatronics*, vol. 18, no. 5, pp. 1498–1507, 2013.
- [46] M. A. Janaideh and D. S. Bernstein, “Adaptive Control of Uncertain Hammerstein Systems with Hysteretic Nonlinearities,” in *53rd IEEE Conference on Decision and Control*, pp. 545–550, 2014.
- [47] K. Kuhnen and P. Krejci, “Compensation of Complex Hysteresis and Creep Effects in Piezoelectrically Actuated Systems—a New Preisach Modeling Approach,” *IEEE Transactions on Automatic Control*, vol. 54, no. 3, pp. 537–550, 2009.
- [48] M. Al Janaideh, M. Rakotondrabe, and O. Aljanaideh, “Further Results on Hysteresis Compensation of Smart Micropositioning Systems with The Inverse Prandtl–Ishlinskii Compensator,” *IEEE Transactions on Control Systems Technology*, vol. 24, no. 2, pp. 428–439, 2016.
- [49] M. S. Rana, H. R. Pota, and I. R. Petersen, “A Survey of Methods Used to Control Piezoelectric Tube Scanners in High-speed AFM Imaging,” *Asian Journal of Control*, vol. 20, no. 4, pp. 1379–1399, 2018.
- [50] S. Roa, N. Haberkorn, and M. Sirena, “Atomic Force Microscopy Nano-indentation For Testing Mechanical Properties in thin Films,” *Materials Today: Proceedings*, vol. 14, pp. 113–116, 2019.
- [51] H. Xie and S. Régnier, “Three-dimensional Automated Micromanipulation Using a Nanotip Gripper with Multi-feedback,” *Journal of Micromechanics and Microengineering*, vol. 19, no. 7, pp. 1–9, 2009.
- [52] A. Bolopion, H. Xie, D. S. Haliyo, and S. Régnier, “Haptic Teleoperation for 3-D Microassembly of Spherical Objects,” *IEEE/ASME Transactions on Mechatronics*, vol. 17, no. 1, pp. 116–127, 2010.
- [53] M. Rakotondrabe, C. Clévy, and P. Lutz, “ H_∞ Deflection Control of a Unimorph Piezoelectric Cantilever under Thermal Disturbance,” in *International Conference on Intelligent Robots and Systems*, pp. 1190–1197, 2007.
- [54] Q. Zhang, H. Wang, N. Kim, and L. Cross, “Direct Evaluation of Domain-wall and Intrinsic Contributions to The Dielectric and Piezoelectric Response and Their Temperature Depen-

- dence on Lead Zirconate-Titanate Ceramics,” *Journal of Applied Physics*, vol. 75, no. 1, pp. 454–459, 1994.
- [55] D.-S. Paik, S.-E. Park, T. Shrout, and W. Hackenberger, “Dielectric and Piezoelectric Properties of Perovskite Materials at Cryogenic Temperatures,” *Journal of materials science*, vol. 34, no. 3, pp. 469–473, 1999.
- [56] A. Benayad, G. Sebald, B. Guiffard, L. Lebrun, D. Guyomar, and E. Pleska, “Temperature Dependence of Piezoelectric Properties of PMN-PT and PZN-PT Single Crystals,” in *Journal de Physique IV (Proceedings)*, vol. 126, pp. 53–57, 2005.
- [57] J. Debus, “Modelling The Behaviour of Single Crystal Devices with ATILA: The Effect of Temperature and Stress on A single Crystal Bar, Tonpiliz and Sphere Submitted to A Harmonic Analysis,” in *Applications of ATILA FEM Software to Smart Materials*, pp. 305–374, 2013.
- [58] S. Liang, M. Boudaoud, B. Cagneau, and S. Régnier, “Velocity Characterization and Control Strategies for Nano-robotic Systems Based on Piezoelectric Stick-slip Actuators,” in *IEEE International Conference on Robotics and Automation*, pp. 6606–6611, 2017.
- [59] M. Rakotondrabe, M. C. Diouf, and P. Lutz, “Robust Feedforward-feedback Control of a Hysteretic Piezocantilever under Thermal Disturbance,” *IFAC Proceedings Volumes*, vol. 41, no. 2, pp. 13725–13730, 2008.
- [60] M. Rakotondrabe and I. A. Ivan, “Development and Dynamic Modeling of a New Hybrid Thermopiezoelectric Microactuator,” *IEEE Transactions on Robotics*, vol. 26, no. 6, pp. 1077–1085, 2010.
- [61] S. Mirjalili, S. M. Mirjalili, and A. Lewis, “Grey Wolf Optimizer,” *Advances in Engineering Software*, vol. 69, pp. 46–61, 2014.
- [62] H. Faris, I. Aljarah, M. A. Al-Betar, and S. Mirjalili, “Grey Wolf Optimizer: A Review of Recent Variants and Applications,” *Neural Computing and Applications*, vol. 30, no. 2, pp. 413–435, 2018.